Geared PM Wind Generator and MPPT Control for DC-Grid Wind Energy System

by

Lethiwe Philile Mdakane

Thesis presented in partial fulfilment of the requirements for the degree of Master of Engineering (Electrical) in the Faculty of Engineering at Stellenbosch University

Supervisor: Prof. M.J Kamper

March 2020

Declaration

By submitting this thesis electronically, I declare that the entirety of the work contained therein is my own, original work, that I am the sole author thereof (save to the extent explicitly otherwise stated), that reproduction and publication thereof by Stellenbosch University will not infringe any third party rights and that I have not previously in its entirety or in part submitted it for obtaining any qualification.

Date: ..... March 2020 .....

Abstract

Geared PM Wind Generator and MPPT Control for DC-Grid Wind Energy System

L.P Mdakane

Department of Electrical and Electronic Engineering,
University of Stellenbosch,
Private Bag X1, Matieland 7602, South Africa.

Thesis: MEng (Elec)

March 2020

In this study a geared PM generator for small-scale DC-grid connected wind energy systems is considered. A commercial 2.2 kW PM generator is evaluated using FEA software and is used for practical system measurements. An alternative 4 kW PM generator that achieves a high torque density and low cogging torque is designed. A simple robust feedforward maximum power point tracking (MPPT) control method is proposed, which is attained through feedback gain-scheduling. A practical set-up of the system is built and practical measurements of the system are taken. It is found, from simulation, that the proposed MPPT control method that is derived is capable of having the system operating at its MPPT trajectory. The practical results show that the duty cycle of the DC-DC converter can be adjusted according to optimum values in order to control the system and have it operating at its MPPT.

Uittreksel

Geratte PM-generator vir kleinskaalse GS-netwerkverbinding windenergie-stelsels

("Geared PM Wind Generator and MPPT Control for DC-Grid Wind Energy System")

L.P Mdakane

Departement Meganiese en Megatroniese Ingenieurswese,
Universiteit van Stellenbosch,
Privaatsak X1, Matieland 7602, Suid Afrika.

Tesis: MIng (Meg)

Maart 2020

In hierdie studie word 'n geratte PM-generator vir kleinskaalse GS-netwerkverbinding windenergie-stelsels beskou. 'n Kommersiële 2.2 kW PM-generator word met behulp van FEA-sagteware geëvalueer en word gebruik vir praktiese stelselmetings. 'n Alternatiewe 4 kW PM-generator met 'n hoë draaimoment digtheid en 'n lae getande draaimoment, is ontwerp. 'n Eenvoudige robuuste vorentoevoer maksimum drywingspunt volging (MDPV) beheermetode word voorgestel, wat bereik word deur middel van terugvoer aanwinsskedulering. 'n Praktiese opstelling van die stelsel is gebou en praktiese metings van die stelsel is gedoen. Vanuit simulasie is gevind dat die voorgestelde MDPV-beheermetode wat afgelei is, die stelsel op sy MDP-baan kan laat werk. Die praktiese resultate wys dat die dienssiklus van die GS-GS-omsetter kan verstel word ooreenkomstig optimum waardes om sodoende die stelsel by MDP te beheer.

Acknowledgements

I would like to acknowledge and express my gratitude to the following people who have played an important role to the success of this study.

- To Jesus Christ, my Lord and saviour, for His faithfullness and unwavering love.
- To my supervisor Professor Kamper for his wisdom, guidance, support and patience throughout the course of this project.
- Everyone from the Workshop, Mr Petzer, Mr Swart, Kenan Cloete, Andrew Loubser and Brent for all your time, patience and willingness to go the extra mile.
- To my colleuges in the research office, who are always willing and happy to offer their help and assistance when needed.
- Finally I would like to acknowledge my mom, family and friends for all your support, prayers, love, always believing in me and always encouraging me to follow my dreams.

Publications

- T. Kanda, L. Mdakane, C. Labuschagne and M. Kamper: Dynamics of maximum power point wind energy battery charging systems. In: 2019 *Southern African Universities Power Engineering Conference/Robotics and Mechatronics/Pattern Recognition Association of South Africa* (SAUPEC/RobMech/PRASA), pp. 576-581. IEEE, 2019.

  Bloemfontein (South Africa), Jan 2019

- L.P Mdakane, M.J Kamper: Simple MPPT control for wind energy dc-grid connected systems. In: 2019 *45th Industrial Electronics Society Conference*, IEEE, 2019.

  Lisbon (Portugal), Oct 2019

Dedication

This thesis is dedicated to my late father Benedict Davidson Sipho Mdakane. You will always be remembered.

Contents

List of Figures

List of Tables

Nomenclature

Variables

v	Voltage	[V]
i	Current	[A]
e	Back-EMF	[V]
λ	Flux linkagge	[Wb – turns]
f	Frequency	[Hz]
n	Mechanical Speed	[r/min]
B	Friction Coefficient	[Nm.s/rad]
R	Resistance	[ ]
L	Inductance	[H]
J	Current Density	[A/mm^2]
J_t	Turbine Inertia	[kg.m^2]
N	Gearbox Ratio	[ ]
p	Poles	[ ]
Q	Slots	[ ]
ω	Angular Velocity	[rad/s]
T	Torque	[N.m]
τ	Time constant	[s]
ρ	Resistivity of copper	[ ]
P	Power	[W]

θ Rotor Angle . . . . . [rad]

Abbreviations

2-D Two Dimensional

AC Alternating Current

DC Direct Current

DFIG Doubly-Fed Induction Generator

EMF Electromotive Force

FEA Finite Element Analysis

FE Finite Element

HAWT Horizontal Axis Wind Turbine

IGBT Insulated-Gate Bipolar Transistor

IG Induction Generator

IPM Intelligent Power Module

LUT Lookup Table

MPPT Maximum Power Point Tracking

OCC] Open-Circuit Characteristic

PCB Printed Circuit Board

PI Proportional Integral

PM Permanent Magnet

PMSG Permanent Magnet Synchronous Generator

PWM Pulse Width Modulation

REIPPPP Renewable Energy Independent Power Producer Procurement Programme

RMS Root Mean Square

SEMFEM Stellenbosch Electrical Machines Finite Element Method

SSC Short-Circuit Characteristic

UMP Unbalanced Magnetic Pull

VAWT Vertical Axis Wind Turbine

WECS Wind Energy Conversion System

Chapter 1

Introduction

Wind as a source of energy dates back many years, where it was initially used to pump water, used by windmills to grind grain and used in propelling ships [1]. The first wind turbine utilized for the generation of electricity was built in 1891 [1]. The development of wind turbine technology has grown immensely since then. Global trends show that the total capacity installed globally has increased from 121 GW to a capacity of 591 GW from the year 2008 to the end of 2018 [2]. This helps to relate how far wind turbine systems have come and that the cumulative capacity is yet to grow even further. There is still a significant gap between the world's top 10 wind energy producing countries and Africa as well of the rest of the countries in the world. Even with this gap, these countries still have potential for growth in the wind energy sector. The Global Status Report 2019 conducted by REN21 showed that Africa and countries from the Middle East have seen a substantial market increase, with South Africa contributing 2.1 GW of onshore wind power capacity [2].

Today wind energy generation has seen major technological advancements and has evolved remarkably over the years. Through the use of turbine blade technology, advanced control methods, intricate power electronics converters and efficient generator design, the overall performance of wind energy systems is constantly improving. One of the many benefits of such advancements include modern wind turbines that are capable of harvesting power from wind sites that have relatively low speeds. In recent years, more research and development has been made towards distributed wind energy systems. Small-scale wind energy systems (generally considered as less than 100 kW) are installed close to the end-user and can be connected to local distribution systems or off-grid in remote/rural locations [3].

In the South African context wind energy has great potential. Wind energy in South has grown from having an installed capacity of 794.4 MW to recently having an installed capacity of 2078 MW [4]. South Africa's Renewable Energy Independent Power Producer Procurement Programme (REIPPPP) has played a prominent role in contributing to the growth seen. It is predicted that the capacity is expected to improve by 2 GW additional in the year 2020 and 2021 [5]. Small-scale wind energy systems can also additionally contribute to the energy access in the country. Such systems are beneficial in that the power generated is produced and distributed independently from a centralised electrical grid and is capable of providing energy access to local farms, schools and communities in urban as well as rural areas in developing countries, thus further contributing to the socio-economic development of the country.

To experience the benefits of such stand-alone systems, it is imperative that these systems operate at their optimum efficiency and that solutions that could potentially solve the challenges commonly faced by these systems are investigated and tested. This study investigates and proposes methods for improving the performance of small-scale stand-alone wind energy systems.

The objective of the remainder of this Chapter is to provide a detailed literature review as well as background information that is useful for the purposes of this study and to briefly introduce some of the main concepts that are used in the wind energy system. Each component and subcomponent is discussed and evaluated. The proposed system of this research thesis is introduced and a brief description of the various parts is given. Furthermore, the reasoning behind the choice of each component is discussed. The rest of the Chapter defines the problem statement, the objectives of the study, the approach to the problem and finally a brief description of the layout of the rest of the thesis.

1.1 Wind Energy Conversion Systems

Wind energy has played a prominent role towards alternative power generation methods [6]. To increase the growth of successful wind generation systems, it is crucial that the design and evaluation of the system is done in a manner that results in the desired performance of the system, in terms of energy production, efficiency and reliability. A typical

wind generator system comprises of a wind turbine, a tower, a generator and the remaining balance of system components such as power electronic converters, wiring, controllers, storage batteries, etc [7].

In wind energy conversion systems (WECSs), the kinetic energy of wind rotates the wind turbine blades generating mechanical energy. This mechanical energy generated from the rotating blades is transferred from the shaft to the rotor of the generator. The mechanical energy is then converted into electrical energy by the generator. Thereafter, the electrical energy is converted and transferred to the grid/load.

Like most integrated systems, certain components play a more prominent role than others, and for a wind generator system the most important component is the electrical drivetrain. The electrical drivetrain in wind energy systems typically consist of the generator, transformer, switch gear and convertors [8]. Hence, great detail and emphasis is put on the design of these sub components. The generator is required to convert mechanical energy produced by the wind turbines into electrical energy. The generator of the system could be a Doubly-Fed Induction Generator (DFIG), a Permanent Magnet Synchronous Generator (PMSG), Induction generator etc. The electrical energy generated from the WECS is then controlled and converted according to the requirements for its use of application and then distributed to a utility grid or off-grid. The WECS investigated in this study is discussed in this Chapter.

1.1.1 Large-scale and small-scale wind energy systems

Large scale wind energy systems are typically used to generate electrical power to be delivered to transmission networks. These systems have a rated power capacity that typically range between 1 MW to 5 MW [9]. Small scale wind turbines are generally designed to be used in agricultural, residential, small commercial and some industrial applications [10]. Small scale wind turbines are attractive in enabling the end-user to offset the use of power from the grid. These small turbines can be connected to the national grid for the generation of electricity, used off-grid for battery storage or water pumping in remote locations, and can also be connected to a DC-grid . Small scale wind turbines generally have power ratings that are less than 100 kW [11]. In this study a small scale wind turbine is chosen since the system is designed for a DC-grid and further be used for battery charging, refer

to 1.3.4 for choice behind DC-grid. Such wind turbine systems are ideal for application in remote locations.

1.1.2 HAWT and VAWT turbine topology

Wind energy systems have many different configurations and can be categorized according to various system topologies. One way is to classify them is in terms of the axis type with which the turbine blade rotates around. The two types of turbine axis configuration are mainly horizontal axis wind turbine (HAWT) and vertical axis wind turbine (VAWT). These two types of turbine topologies are shown in Fig. 1.1. As discussed in [1], the main advantage of VAWTs is that they are easy to service and maintain, since the generator and the gearbox are located on the ground [12]. Another advantage is that they do not require control of the yaw. On the other hand the disadvantage of VAWTs is that the blades are placed close to ground and mostly exposed to lower wind speeds [1].

In industry most modern large wind turbines are of the HAWT type. The comprehensive review comparing vertical axis and horizontal wind turbines carried out in [13], states that HAWTs are advantageous in that the blade pitch of these turbines are adapted according to the wind. Furthermore, HAWTs are attractive since they have high towers that can reach more powerful wind speeds and have a higher efficiency when compared to

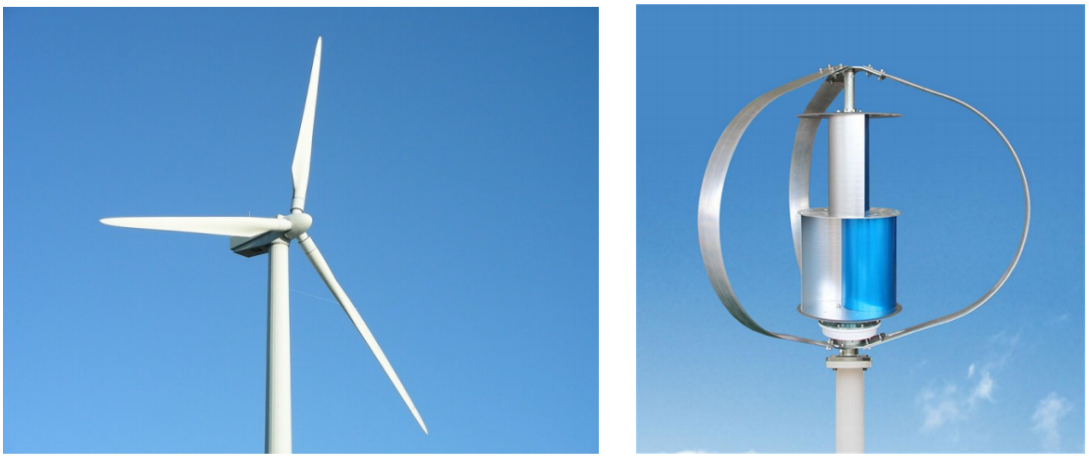

(a) A typical HAWT wind turbine. (b) A VAWT wind turbine.

Figure 1.1: Typical turbine topology.

VAWTs. The main disadvantages of HAWT is the need for yaw control systems to have the blades turn in the direction of the wind and require high maintenance. However, the study done by [13], deduced that HAWT are overall better than VAWT in terms of efficiency, maximum output power and implementation. The VAWT has not been as commercially successful as HAWTs. This is due to issues of reliability and poor performance. HAWT on the other hand are known to be economically viable and more attractive for commercial use because they are more advanced and reliable. Therefore, a HAWT is considered in this study.

1.1.3 Variable-pitch turbines and fixed-pitch blade turbines

Another way to categorize wind energy systems is by considering whether the turbine blades are orientated at a fixed or variable angle towards the incoming wind. Variable-pitch turbines actively control the angle of rotor blades according to the changes in the wind speed [14]-[15]. Fixed-pitch turbine blades are positioned onto the hub at a fixed angle. In this thesis, the wind turbine used is a fixed-pitch turbine, as shown in Fig. 1.2, and was chosen based on the available power-speed characteristic curve obtained from existing fixed-pitch turbine. The power-speed characteristic curve are given in Fig. 1.3. At different wind speeds, the fixed turbine blades generate mechanical output power as a function of the rotating speed of the turbine. This turbine power is shown in Fig. 1.3 for the various wind speeds. The first operating point of the turbine, as seen in the figure, is the cut-in speed of this turbine which is 100 r/min occurring at the minimum wind speed of 3 m/s at which the turbine starts to generate power. This cut-in speed is the rate at which the starting torque of the turbine is achieved. The second turbine operating point is the rated operating point of the turbines rated power, which occurs at a wind speed of 12 m/s correlating to a turbine speed of 320 r/min and a rated power of 5 kW.

1.1.4 Direct-drive and indirect-drive

In wind generation systems, the wind turbine can either be directly connected to the wind generator or connected via a gearbox. The first connection type is known as direct-drive and is often implemented to reduce the mechanical losses in the system [16]. The geared connection type is typically used in instances where the generator is required to rotate at a higher speed than the wind turbine. The disadvantage of this type of configuration is that the gearbox requires maintenance which may raise issues of cost and it contributes

Figure 1.2: Wind turbine at test site.

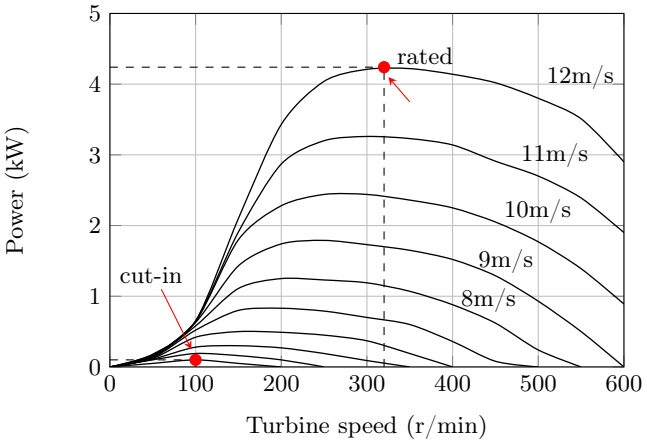

Figure 1.3: Wind turbine power-speed characteristic curve.

to the overall system losses [17]. The system implemented in this study makes use of the indirect-drive configuration. The advantage of the geared option is a smaller generator and much less magnet material used.

1.2 Proposed System

The wind turbine system proposed in this thesis is shown in Fig. 1.4. The system considered for the study consists of a small-scale (2.2 kW) permanent magnet synchronous generator (PMSG) for fixed-pitch wind turbines and is designed for medium voltages (400 V) for relatively long transmission distances. The PMSG is mechanically connected to the

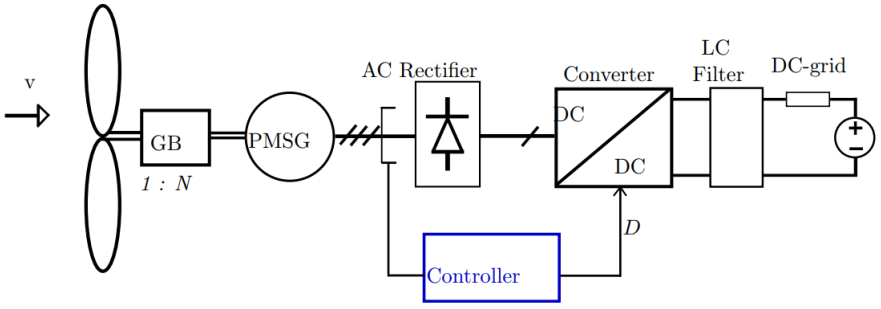

Figure 1.4: Layout of PM wind generator system connected to a DC-grid.

gearbox and connected electrically to a 3-phase full-bridge diode rectifier. The rectifier is then connected to a DC-grid through an LC filter of the DC-DC converter. The system further includes the implementation of a proposed feedforward control mechanism to ensure MPPT of the system. The system proposed similarly follows the topology presented by [18], [19] and [20], however is different in terms of the analysis, objectives for the system and the methodology.

1.3 System Components

1.3.1 Permanent Magnet Synchronous Generator

There are various generator types used in wind energy systems. In small-scale wind turbine systems, two of the most common generators used is the induction generator (IG) and the permanent magnet synchronous generator (PMSG) [21].

The PMSG is generally more preferred for small-scale wind turbine systems over other generator topologies. They are known to have high efficiency and a high torque density [16]. The PMSG does not require slip-rings and brushes which contributes in them having lower maintenance costs. In addition there is no requirement for external power supply to excite the field of the generator [22]. Although it is a conventional machine, the PMSG is well suited for application in small-scale turbine systems.

1.3.2 DC-DC Converter

Power electronics play a prominent role in renewable enegry systems. In wind energy systems, power electronics are typically used for power conversions, e.g. converting AC power to DC power and vice versa, for control methods and are also used for sensors and measurements. The disadvantages of power electronics is that they can be quite expensive, they are prone to failure in severe operating conditions and give rise to non-sinusoidal currents [23].

In this research study, a DC-DC switching converter is used and it forms the interface between the generator and the DC-grid through a diode rectifier. There are various topologies used for DC-DC converters for different applications such as a buck, boost, bidirectional, cÃºk and full-bridge topologies [24]. The Buck (step-down) topology is chosen for the

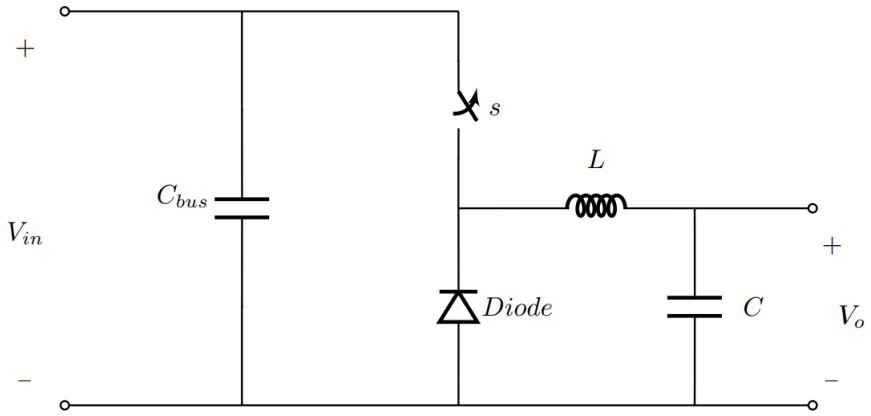

Figure 1.5: Circuit diagram of Buck converter topology.

converter in order to step-down the medium voltages of the generator to a lower voltage that corresponds to the DC-grid voltage requirement. The topology of the converter used is shown in Fig. 1.5. The DC-DC converter is connected between the rectifier output and the DC-grid.

The DC-DC converter can be implemented in wind energy systems for power matching by continually adjusting the DC-bus voltage as the rotating speed of the wind generator changes, which in effect allows the generator to follow its maximum power point trajectory. The control input of the converter is given by a pulse width modulated signal to trigger the switching of the converter to effectively control the system to achieve maximum power point tracking. According to [25], a DC-DC converter can be utilised for MPPT and this concept can be achieved in a feedforward control manner, by controlling the duty cycle and adjusting it in relation to the measured rotational speed of the generator. The application of the DC-DC converter for the aforementioned purposes is implemented in Chapter 5. The DC-DC converter used in the project is further discussed and evaluated in detail in Chapter 2.

1.3.3 MPPT Control Methods

Tracking the maximum power harvested is essential in wind turbine systems that have sources that generate variable power. Maximum power point tracking aims to maximize the amount of power that can be extracted by a system while improving the efficiency of

energy conversion systems. There are a number of different ways maximum power point tracking can be achieved. The four main MPPT control methods that are most commonly used are perturb and observation, optimal torque control, tip speed ratio control and power signal feedback control [26]. Other MPPT control methods implemented are namely sliding mode control, extremum seeking control, fuzzy logic control, steepest ascent method and particle swarm optimization [27].

From literature reviewed, the method put forward in [28] implements a combination of sliding mode and extremum seeking control. In [29], the steepest ascent method is applied to maximise the generator power by adjusting the duty cycle of the converter according to the difference between successive output power measurements. In a more recent study conducted in [30], a MPPT method based on particle swarm optimization is used to observe the system's response to low wind speeds and high wind speeds. The study however, does not look at the system's response to wind speeds occurring at different frequencies. The MPPT methods mentioned have proven to be valid however, many of them rely on complex algorithms and intricate implementation. Furthermore, it is not clear whether the wind energy systems maintain stability in response to wind speed disturbances.

Each of the methods are proven to work well, and have some advantages and disadvantages. The implementation of complex algorithms often comes with added costs required for the implementation of these technologies. In this research study, a control method is proposed that moves away from the use of intricate algorithms by implementing a very simple control method to achieve MPPT. This method uses feedforward control by means of controlling the duty cycle of the DC-DC converter in relation to the measured generator speed. The advantage of using this control method for MPPT is that the practical implementation of the method is fairly simple since only a measurement of the generator-voltage's frequency is required, or alternatively a measurement of the DC-link voltage is required.

The feedforward MPPT control method proposed is in essence attained through a form of feedback-gain scheduling. Furthermore the proposed method is attractive for industry application since PI-torque, speed and current regulators are not necessary. The method is further discussed and explained in great detail in Chapter 5.

1.3.4 DC-Grids

Alternating current (AC) power grids are used by the utility and form the interconnected network that is responsible for the distribution of electrical power to consumers. As the power demand continues to increase due to rapid population growth, the quality of the electrical power and reliability delivered by conventional AC distribution grid has decreased due to high demands from the population. The AC distribution network operations and intended expansions are limited as a result of transmission line damages, a lack of line capacity and shortage of power supply channels to improve the infrastructure [31].

Distribution grids are generally used to deliver electricity to the end-user. They form part of the last stage of the electrical grid once electricity has been transmitted from power generation. In distributed grids, the power generation from renewable energy can be obtained through solar, hydro, wind energy or hybrid systems [32]. Distributed grids can be connected to the normal conventional utility grid or can have an off-grid topology. Off-grid systems do not rely on the utility grid but work as standalone systems. Such offgrid systems are useful and convenient for application in remote rural areas where there is insufficient infrastructure from the utility grid [32]. A typical topology of a DC-grid is given in Fig. 1.6.

DC-grids are an alternative to conventional AC power utility grids, and as a result have

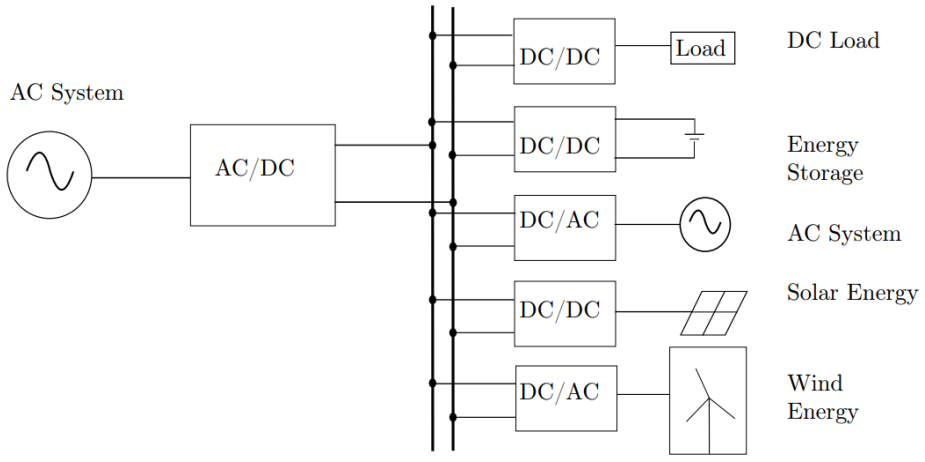

Figure 1.6: Layout of typical DC-grid topology.

gained a large amount of attention from industry in recent years. Such power grids are advantageous in that they help improve the power quality, the stability, and control of power systems [33]. Hence, DC-grids are capable of solving some of the problems that exist in the current traditional AC utility power grids. DC-grids contribute in facilitating more integration of renewable energy sources. One of the challenges faced by DC-grids, is rapid detection and isolation of DC faults [34]. This problem has been mitigated by developments in DC breaker technologies [35]. Another concern for DC-grids is the instability of the DC bus voltage in response to fluctuation of wind energy. The problem can be resolved through bidirectional energy flow control using a DC-DC converter and supercapacitors[33]. It can be mentioned here that the MPPT control method proposed in Chapter 1.3.3, is found to be insensitive to such DC-grid variations.

The wind energy system proposed is connected to a DC-grid and the DC-grid is modelled as a battery as shown in Fig. 1.4.

1.4 Problem Statement

Small-scale stand-alone wind energy systems are advantageous in that they require lower costs to install and they can be located in rural or remote areas. With advancement in wind technology, wind power can be harvested at low wind speeds. To ensure optimum performance and high efficiency, control methods are generally used to maximise the conversion process of WECS that converts the kinetic energy of wind into rotational mechanical energy of the wind turbine. This is achieved through maximum power point tracking control methods. Furthermore, the effectiveness in electrical synchronous generator having low cogging torque and high torque density is ideal in ensuring an efficient wind energy system.

However, a number of challenges are faced with implementing such a system. Firstly, most of the MPPT control methods require intricate and complex algorithms which are difficult to implement due to the need of PI-torque, speed and/or current regulators [36]. Secondly, most of the rural regions in South Africa do not have access to established infrastructure for utility grids or centralised generation systems. As a result, this leaves a small portion of the country still unelectrified. The third challenge is the well-known effects that exist from cogging torque in permanent magnet machines which are undesirable. The effects of cogging torque negatively impact the performance of the machine due to the

presence of noise, vibrations as well as increasing the overall output torque ripple observed [37]. Furthermore, a low cogging torque of the machine is ideal in instances when the operating wind speeds of the wind turbine are low [23].

In response to some of these challenges, this research study proposes to investigate and develop several potential solutions to the problems mentioned above.

1.5 Approach to Problem

In this study, a stand-alone small-scale wind turbine system is considered. An existing 6-pole 2.2 kW planetary geared PMSG is investigated and simulated using finite element analysis and further used for the practical measurements of the system. An alternative 8-pole 5 kW PMSG is designed using finite element analysis, to increase the torque density of the generator and further decrease the cogging torque through the use of fractional-slot windings. A simple control method for MPPT that has a DC-DC converter under duty cycle control is proposed. The method does not require complex algorithms but makes use of an optimum duty cycle, as developed in Chapter 5, to control the system to slide the turbine along its maximum power trajectory. Lastly, practical tests and measurements are to be made to confirm the accuracy of the simulated machine and test the practical application of the proposed MPPT control method.

1.6 Objectives of Study

The following objectives are aimed to be accomplished through this study:

- An existing PMSG is simulated through finite element analysis software packages SEMFEM and ANSYS Maxwell by using the physical dimensions of the machine to model it. The parameters of the machine are calculated according to the FEA simulation results and compared to the theoretical analysis.
- Design of an alternative PMSG that achieves a high torque density and low cogging torque is made using finite element analysis software packages SEMFEM and ANSYS Maxwell.

- A simple control method to achieve MPPT for wind energy DC-grid connected system is proposed, developed and evaluated.
- Practical set-up of the wind energy system connected to a battery bank to emulate DC-grid for testing the PMSG and evaluating the proposed control method.
- Discussion and interpretation of simulation results and practical results.

1.7 Thesis Layout

Chapter 1: This Chapter looks at the historical development of wind power, the current trends in wind energy and problems put forward from literature are discussed.

Chapter 2: In this Chapter, the description of the system implemented in this study is given in detail. The system specification and parameters are given, as well as the mathematical modelling of the various system components.

Chapter 3: The PM synchronous generator used in this study is simulated and analysed using finite element analysis.

Chapter 4: An alternative design of the PM generator is further proposed. Finite element analysis is performed to simulate the generator.

Chapter 5: In this Chapter, a MPPT control method is proposed and developed. The control method is simulated using MATLAB Simulink software. Furthermore, the dynamics of the system are investigated and the simulated results of the wind energy system are given.

Chapter 6: The results of the measurements obtained from the practical test are given and discussed in this chapter.

Chapter 7: Conclusions drawn from the project are discussed and future recommendations are put forward.

Chapter 2

System Description and Analysis

In this Chapter, the mathematical modelling and theoretical analysis of the wind turbine, gearbox, PMSG, DC-DC converter and the DC-grid is discussed. The equations governing each component are given. The mathematical derivation for the steady-state equivalent circuit model and dq-model of the PMSG are presented. The equations used to design the DC-DC converter are given, as well as the approach used in modelling the DC-grid model.

2.1 Wind Turbine

Due to the non-linear nature of wind turbines, the process of modelling wind turbines is rather complex. Hence, the HAWT wind turbine of the system, as shown in Fig 1.2, is modelled as a functional generator. The functional generator consists of two inputs, the wind speed and turbine speed, and has one output which is the turbine torque. The functional generator used to model the turbine is implemented in MATLAB Simulink in the form of a look-up table (LUT). In the LUT, the values of the power-speed characteristic curves are used to interpolate the corresponding output torque of the turbine, according to the given inputs of wind speed and turbine speed. Thus, the turbine power can be determined from the turbine torque which forms the output of the functional generator from this equation

$$P_t = \omega_t T_t, \tag{2.1}$$

where P_t is the turbine power and is calculated using T_t determined from the turbine power curves occurring at a specific wind speed v and turbine speed ω_t. A block-diagram describing the wind turbine model is given in Fig. 2.1. The turbine torque is then fed to

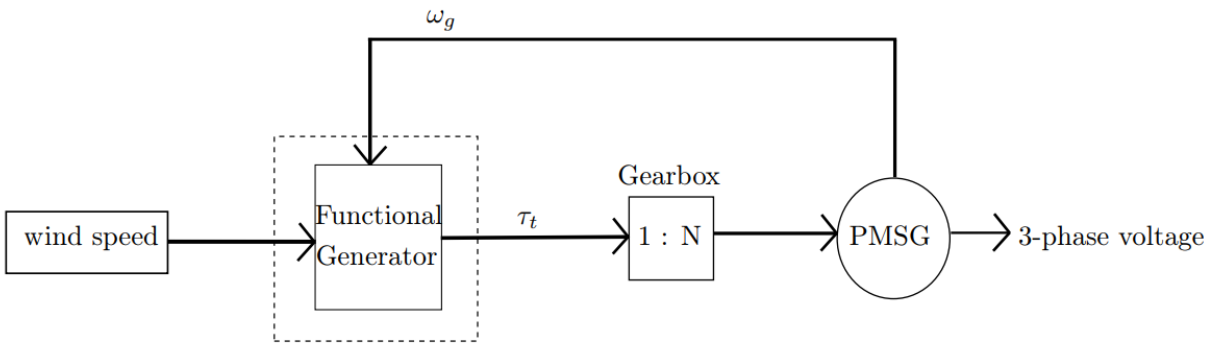

Figure 2.1: Block diagram of wind turbine model.

the PMSG of the system.

The dynamics of the mechanical system is governed by differential equation given as

$$T_t - T_g = J_t \frac{d\omega_g}{dt} + B\omega_g, \tag{2.2}$$

where J_t is the inertia of the wind turbine, $\omega_g = N\omega_t$ and B is the rotational damping coefficient. The mechanical time constant for the mechanical part of the system is determined as

$$\tau_m = \frac{J_t}{B}. \tag{2.3}$$

The value of B is relatively small therefore the mechanical time constant τ_m is considered to be very large.

2.2 Gearbox

The wind turbine is mechanically connected to a planetary gearbox. The gearbox has a ratio of $N = 1 : 7$ and is then mechanically connected to the PMSG. The gear train of the gearbox increases the speed between the wind turbine and PMSG. When the system is considered on the high speed side of the gearbox, equation (2.2) becomes

$$T_t' - T_g = J_t' \frac{d\omega_g}{dt} + B\omega_g. \tag{2.4}$$

Equation (2.4) is used to model the dynamics of the turbine and the gearbox, where the superscript (') denotes the high speed side of the gearbox.

2.3 PM Generator

In a PMSG, the magnetic flux in the rotor is generated by the permanent magnets mounted on the rotor. A rotating magnetic field is produced as the rotor rotates with the shaft. A three-phase voltage is thus induced in the stator windings of the generator. The PM machine is a synchronous machine which means that the rate at which the electrical frequency of the generator is produced, is done at the same mechanical rate at which the generator shaft rotates. The mechanical rotational speed of the rotor is related to the electrical frequency of the stator as

$$f_e = \frac{n_m p}{120}, \tag{2.5}$$

where n_m is rotational speed of the rotor, P is number of poles of the machine and f_e is the electrical frequency of the stator.

2.3.1 Equivalent Circuit

The analysis of the PMSG can be simplified by means of an equivalent circuit for a single phase of the three-phase synchronous generator. The per-phase equivalent circuit of the generator is shown in Fig. 2.2. The equivalent circuit of the synchronous generator is derived by knowing that the flux-linkage of phase-a is dependent on the rotor angle and is a function of time given as,

$$\lambda_a = L_s i_a + \lambda_{pm}, \tag{2.6}$$

where L_s is the synchronous inductance, ia is the armature current and λ_{pm} is the fluxlinkage produced by the permanent magnets.

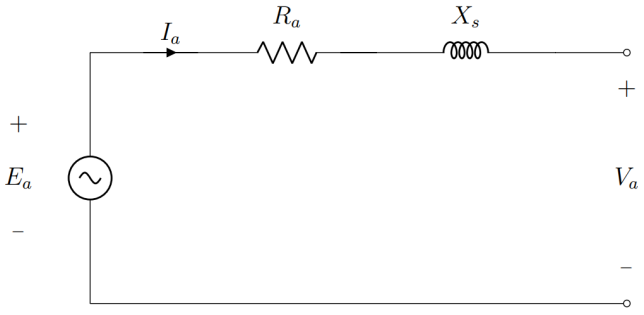

Figure 2.2: Synchronous generator per phase equivalent circuit.

The voltage induced by the magnets is derived by taking the time derivative of (2.6) with ia equal to zero. The time derivative of (2.6) results in $\lambda_a = \lambda_{pm}$. Thus, the induced voltage can be determined as

$$e_a = \frac{d}{dt}\lambda_a = \frac{d}{dt}\lambda_{pm}. \tag{2.7}$$

The terminal voltage of phase-a is determined by summing the voltage drop across the armature resistance R_a as well as the induced voltage. The terminal voltage is thus expressed as

$$\begin{aligned} v_a &= R_a i_a + \frac{d\lambda_a}{dt} \\ &= R_a i_a + L_s \frac{di_a}{dt} + e_a. \end{aligned} \tag{2.8}$$

The electrical time constant τ_e for the electrical part of the system is determined from (2.8), as

$$\tau_e = \frac{L_s}{R_a}. \tag{2.9}$$

The induced voltage e_a is generated at a frequency ω_e and its amplitude is given as an RMS value by

$$E_a = \frac{\omega_e \lambda_{pm}}{\sqrt{2}}, \tag{2.10}$$

where $\omega_e = 2\pi f_e$. Under steady-state synchronous operating conditions, the equivalent circuit is expressed mathematically by expressing the terminal voltage in terms of its complex RMS magnitude values as

$$V_a = -R_a I_a - jX_s I_a + E_a, \tag{2.11}$$

where X_s is the synchronous reactance. The synchronous reactance, comprising of the armature leakage reactance and the magnetizing reactance, is given by

$$X_s = j\omega_e L_s. \tag{2.12}$$

2.3.2 The dq0 Transformation

The dq0 transformation is applied and used to determine the governing equations used to express a synchronous machine in terms of its dq0 quantities. The transformation is useful in transforming the time-varying inductance seen by the stator phases into quantities which rotate in synchronism with the rotor and hence see constant magnetic paths

[38]. This helps simplify the analysis of the interaction between rotor and stator flux mmf waveforms.

By applying the dq0 transformation, the flux-linkage is expressed in simplified terms of dq0 variables as

$$\begin{aligned} \lambda_d &= L_d i_d + \lambda_{pm} \\ \lambda_q &= L_q i_q, \end{aligned} \tag{2.13}$$

where λ_d and λ_q are the flux-linkages in the direct-axis and quadrature-axis, respectively. The quantities L_d and L_q are the direct-axis and quadrature-axis synchronous inductances respectively, and i_d and i_q are the currents in the direct-axis and quadrature-axis, respectively. With the dq0 transformation applied, the voltage equations result in

$$\begin{aligned} v_d &= -R_a i_d + \frac{d\lambda_d}{dt} - \omega_e \lambda_q \\ v_q &= -R_a i_q + \frac{d\lambda_q}{dt} - \omega_e \lambda_d + \omega_e \lambda_{pm}, \end{aligned} \tag{2.14}$$

for PMSG, where ω_e is the rotor electrical angular velocity. The dq-equivalent vector diagram is shown in Fig. 2.3. Lastly the electromagnetic torque, T_{mech}, for generator can be obtained from

$$T_{mech} = -\frac{3}{2}\left(\frac{p}{2}\right)(\lambda_d i_d - \lambda_q i_d). \tag{2.15}$$

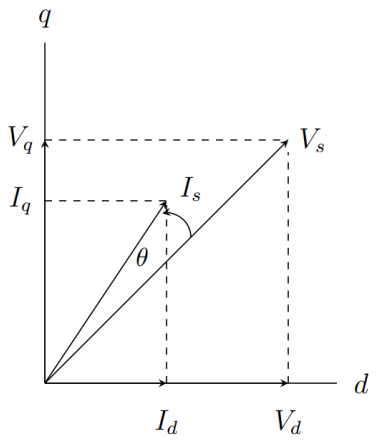

Figure 2.3: Per phase phasor diagram of PMSG.

The equations presented in this section form the fundamental basis used to rotate the reference frame of AC waveforms into DC waveforms with the aim of simplifying the analysis of synchronous machines.

2.3.3 Performance Calculations

This section of the Chapter describes how the d-axis and q-axis equivalent circuit parameters are determined while taking into account the stator copper losses as well as the core losses of the generator. The two equivalent circuits in relation to the d- and q-axes are shown in Fig. 2.4.

In Fig. 2.4, Rs is the stator winding resistance and L_e is the endwinding leakage inductance. Both of these parameters are calculated by means of analytical formulas. The value of the stator winding resistance per phase, R_s, can be determined from,

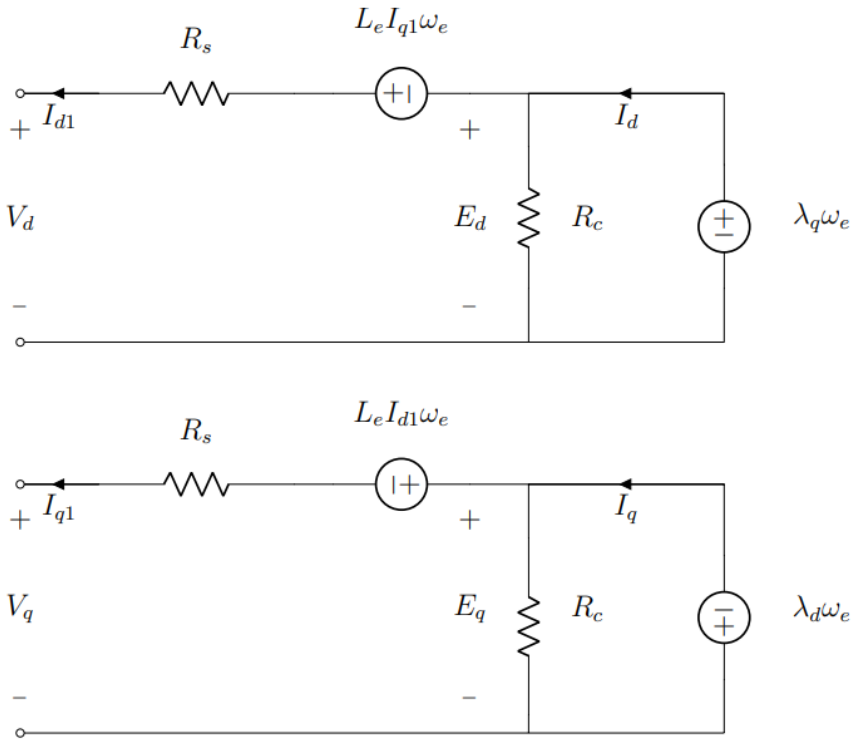

Figure 2.4: Steady-state d- and q-axis equivalent circuits.

$$R_s = \frac{2W^2}{q\frac{p}{2}}(\frac{\rho_t(l+l_e)}{A_{cu}}), \tag{2.16}$$

as demonstrated in [39], where W is the number of turns in series per phase, q is the number of slots per phase per pole, ρ_t is the resistivity of copper, A_{cu} is the active copper area and l_e is the average length of a coil end.

The formula used to determine the endwinding leakage inductance is a formula derived in [39] and adapted for elliptical-shaped coils. The formula is

$$L_e = Vmd_i(\frac{Wk_dk_p}{\frac{p}{2}})^2k_e\text{x}10^{-8}, \tag{2.17}$$

where k_d is the ordinary distribution factor, k_p is the endwinding pitch factor for elliptical-shaped coils, k_e is the endwinding factor for a 3 pole-pair machine, V is the shape factor for single-layer windings, m is the number of phases and d_i is the inner diameter of the stator. The values of k_d and k_p are determined by equations from [40].

The last parameter of the equivalent circuit that is required, is the core loss resistance. This parameter is quite often hard to determine in an accurate manner. To determine the core loss resistance, the stator core losses have to be calculated first. Equation (2.18) is a simple alternative iron loss equation. The simplified formula, as used by [39], is

$$P_{core} = cf_1^x(B_{mt}^yM_t + B_{my}^yM_y), \tag{2.18}$$

where B_{mt} and B_{my} are the maximum flux densities in the teeth and yoke of the machine respectively, M_t is the iron mass of the teeth, M_y is the iron mass of the yoke and f_1 is the fundamental supply frequency. The constants c, x and y are determined from core loss-frequency curves with respect to the specific steel used. The values used to determine these parameters in this study were taken from [39]. Once the core loss is determined, the core loss resistance can be calculated a

$$R_c = \frac{3E_a^a}{P_{core}} \tag{2.19}$$

where, E_a is the RMS value of the phase EMF which is given by the equation

$$E_a = \sqrt{\frac{E_d^2 + E_q^2}{2}} \tag{2.20}$$

and E_d and E_q are clear from Fig. 2.4. The supply voltages of the dq components, as seen in Fig. 2.4, can be calculated from

$$\begin{aligned} V_d &= -R_s I_{d1} - L_e I_{q1} \omega_e + E_d \\ V_q &= -R_s I_{q1} - L_e I_{d1} \omega_e + E_q \end{aligned} \tag{2.21}$$

where the currents I_{d1} and I_{q1} in (2.21) are defined as

$$\begin{aligned} I_{d1} &= I_d + \frac{E_d}{R_c} \\ I_{q1} &= I_q + \frac{E_q}{R_c} \end{aligned} \tag{2.22}$$

Subsequently the amplitude of the current, I_s, and voltage, V_s, are calculated from the following equation

$$\begin{aligned} I_s &= \sqrt{I_{d1}^2 + I_{q1}^2} \\ V_s &= \sqrt{I_{d1}^2 + I_{q1}^2} \end{aligned} \tag{2.23}$$

The consideration of losses in a machine is vital in determining the efficiency of the machine. The voltage drops and current components that contribute to the supply of losses also need to be considered in the representation of machine models. The losses can cause temperature rises that can affect the maximum power that can be reached without the decay of the machine's insulation [41]. The two power losses that are to be considered are the stator copper losses, P_{cu}, as well as the core losses, P_{core}. The core losses are calculated by (2.18) and P_{cu} is determined from

$$P_{cu} = 3 I_{rms}^2 R_s. \tag{2.24}$$

The efficiency of the machine can be expressed as

$$\eta = \frac{P_{out}}{P_{in}}, \tag{2.25}$$

where the input power, P_{in}, and output power P_{out} are given by

$$\begin{aligned} P_i n &= \omega_{me} T_{mech}, \\ P_{out} &= P_{in} - P_{loss} \end{aligned} \tag{2.26}$$

respectively, where P_{loss} is the sum of P_{cu} and P_{core}.

Table 2.1: DC-DC Converter Design Specifications.

Parameter	Value
Input Voltage, V_{in}	73-400 V
Output Voltage, V_o	48 V
Output Power, P_{out}	4.2 kW
Max Output Current, I_o	87.5 A
Switching frequency, f_s	10 kHz
Inductor Ripple Current, ΔI_L	22 %
Capacitor Voltage Ripple, ΔV_{out}	1 %
Duty Cycle, D	0.1 - 0.9

The rotational losses P_{rot} in the system consists of the losses from the gearbox $P_{gearbox}$, the wind-and-friction losses P_{w+f} and the core losses P_{core} of the PMSG, thus the rotational losses are modelled as,

$$P_{rot} = P_{gearbox} + P_{w+f} + P_{core}. \tag{2.27}$$

The rotational losses P_{rot} can be determined in terms of the mechanical damping coefficient B by the following

$$P_{rot} = B\omega_g^2, \tag{2.28}$$

where B is determined from analytical loss calculations.

2.4 DC-DC Converter

The DC-DC converter is connected between the full-bridge diode rectifier and a DC-grid. The converter used is a Buck converter, as mentioned in Section 1.3.2, and is used to step the DC-link voltage from the rectifier down to 48 V of the DC-grid. The circuit diagram of the buck converter can be seen in Fig. 1.5 of Chapter 1. The DC-DC converter was designed and built for the purposes of this study by [20]. The design requirements that the converter was designed and built for are given in Table 2.1. In this system, the converter is used to maintain the output voltage (48 V) of the DC-grid as well as to track the maximum power point of the turbine by controlling the switching of the converter. When the DC-DC converter is assumed to be ideal it can be modelled as a transformer and the following assumptions are true

$$P_{in} = P_{out}, \tag{2.29}$$

$$V_o = DV_{in}, \tag{2.30}$$

$$I_o = \frac{I_{in}}{D}, \tag{2.31}$$

where D is the variable gain. These assumptions are further used in Chapter 5 for the steady-state system analysis for the proposed MPPT control method.

2.4.1 Parameter Calculations

An Intelligent Power Module was used for the DC-DC converter which was designed and built in the Machines Laboratory at Stellenbosch University, shown in [20]. The equations used to design the DC-DC converter are given in the follwing sub sections. The parameter values designed for the DC-DC converter are tabulated in Table 2.2.

2.4.1.1 DC-link Capacitor

A DC bus capacitor is connected between the rectifier and the input of the DC-DC converter. The bus capacitor ensures that the voltage from the diode rectifier that is connected to the DC-DC converter maintains a constant DC voltage by minimizing the voltage ripple. The value of the bus capacitor can be calculated from (2.32) derived by [42].

$$C_{bus} = \frac{I_{dc} D_{max}}{\Delta V_{in} f_s}, \tag{2.32}$$

where I_{dc} is the maximum output current, D_{max} is the maximum duty cycle, ΔV_{in} is the maximum voltage ripple and f_s is the switching frequency of the IGBTs.

2.4.1.2 Snubber Capacitor

Sunbber capacitors are required to remove the voltage spikes and damp the ringing that occurs across the IGBT switches due to the resonance that results from parasitic inductances. The following equation was used to calculate the value for the snubber capacitor

Table 2.2: Design Values for DC-DC Converter.

Parameter	Value
C_{bus}	2 200 uF
$C_{snubber}$	2.2 uF
L	180 uH
C	600 uF

[43],

$$C_{snub} = \frac{L_w i_o^2}{(v_{snub} - v_{dc})}, \tag{2.33}$$

where v_{snub} is the peak voltage of the snubber capacitor, v_{dc} is the maximum supply voltage to the converter, i_o is the maximum output current and L_w is the maximum wiring inductance.

2.4.1.3 LC Filter

The following equations were used to calculate the inductor and capacitor values for the LC filter of the DC-DC Converter, which helps in removing unwanted noise and minimise the voltage ripple in the output [24].

$$L = \frac{D(V_{dc} - V_o)}{f_s \Delta I_L} \tag{2.34}$$

$$C = \frac{V_o(1 - D)}{8 \Delta V_o L (f_s^2)} \tag{2.35}$$

Where V_{dc} is the input DC-link voltage, V_o is the output voltage of the converter, f_s is the switching frequency, ΔI_L is the inductor current ripple, ΔV_o is the capacitor voltage ripple and D is the value of the duty cycle.

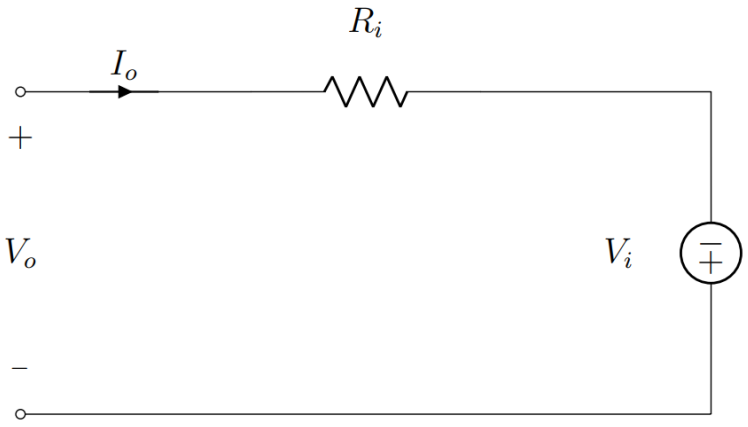

Figure 2.5: Equivalent circuit of DC-grid model.

2.5 DC-grid

The DC-grid of the system is implemented as a battery bank for the practical application of the study. The output of the DC-DC converter is connected to the battery bank. The battery bank that is used to model the DC-grid is made up of four 12 V Lead-acid batteries forming a constant battery bank voltage of 48 V. The constant voltage method is used to charge the rechargeable batteries. The equivalent circuit of the battery bank is shown in Fig. 2.5. The equivalent circuit models the DC-grid as a voltage source V_i in series with a resistor R_i. From this model, the equation expressing the DC-link voltage V_o between the output of the DC-DC converter and the modelled DC-grid is given as

$$V_o = R_i I_o - V_i, \tag{2.36}$$

where V_o and I_o are the output voltage and output current of the DC-DC converter respectively. R_i is the internal resistance of the DC-grid, and V_i is the DC-grid voltage.

Chapter 3

Generator FE Analysis

In this chapter, a theoretical and finite element analysis was conducted on an existing commercial PM generator. A brief description of the machine and the machine's measured dimensions are given. The machine was modelled using two FEM software packages, namely SEMFEM and ANYSYS Maxwell. The results of the simulations generated from the two software packages are then analysed and compared. Finally, conclusions are drawn on the accuracy of the simulation results compared to the theoretical calculations.

3.1 PMSG Description and Dimensions

An existing SEW-Eurodrive 2.2 kW, 6-pole surface mounted PMSG is used for the study. The generator is mechanically connected to a planetary gearbox having a gearbox ratio of 1:7. The generator has a 6/36 pole/slot combination and a rated speed of 3000 r/min. The stator of the generator has a single layer, overlap copper winding and is shown in Fig. 3.1. The existing machine was opened up and disassembled to obtain the machine dimensions and determine the winding layout. The measured dimensions of the generator are tabulated in Table 3.1. A detailed technical drawing of both the stator and rotor of the machine can be found in Appendix A. The rated values of the machine are summarized in Table 3.2.

Figure 3.1: 6-pole PMSG with overlap winding.

Figure 3.2: Rotor of PMSG.

3.2 Modelling and Simulation Results

3.2.1 Machine Modelling in SEMFEM

The generator was modelled and evaluated in SEMFEM, which is an in-house FE program developed at Stellenbosch University. A 2-D drawing of the cross-section of the machine was constructed in SEMFEM according to the dimensions given in Table 3.1. The full model geometry of the generator is shown in Fig. 3.3, where the rotor is drawn to match

Table 3.1: Generator Dimensions.

Machine Parameter	Value
Stator Outer Diameter	105.1 mm
Stator Inner Diameter	61.9 mm
Rotor Diameter	60 mm
Stack Length	120 mm
Number of Slots	36
Number of Poles	6
Air Gap Length	0.95 mm
Number of Winding Layers	1
Coil Span	5

Table 3.2: Rated Nameplate Values of SEW-EURODRIVE PM Generator.

V (line-line)	Hz	r/min	A	Nm	kg
400	150	3 000	6.2	9.5	18.134

the hexagon shape of the actual geometry of the generator's rotor. To run the simulation, a construction of the model geometry is required which in turn becomes the input to the mesh generator. The input 2-D drawing of the model geometry of the generator used in the simulation is shown in Fig. 3.4, alongside the output mesh generated which is shown in Fig. 3.5. Mesh operations are then assigned to the model, allowing the elements to be divided into smaller parts to ensure accuracy and a refined analysis of the generator.

Since SEMFEM executes simulations that are current driven, an input peak phase current is assigned to each of the coils to run the simulations. The FE program then generates the torque, flux-linkages, core losses and copper losses as output variables. The current assigned for the simulation was chosen as $I = 6$ A. A coil span of 5 is used for the overlap winding layout. Prior to the analysis of the model, it is necessary to initially align the position of the rotor in relation to the stator. The flux-linkage of phase-a is a maximum when the position of the rotor d-axis is aligned with the axis of phase-a [38]. The number of turns per coil of the machine were unknown. To ensure that the simulation closely matches the existing machine, an estimate of the number of coil turns had to be determined. To estimate this value for the number of coil turns that are required to closely match the physical machine as much as possible, the value is first assumed and then adjusted itera-

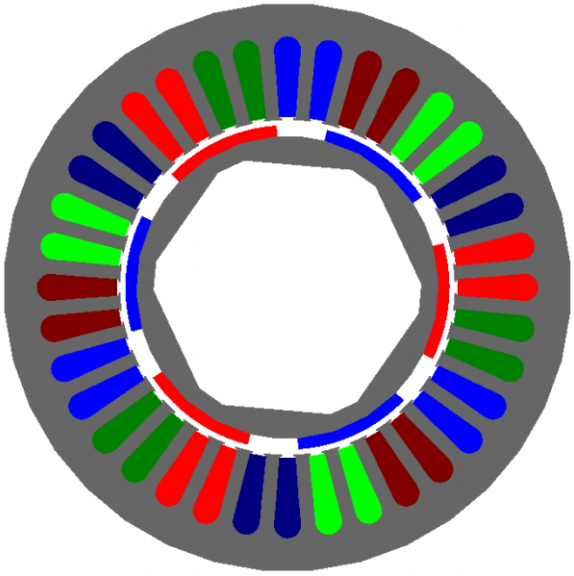

Figure 3.3: 6-pole PMSG with overlap winding.

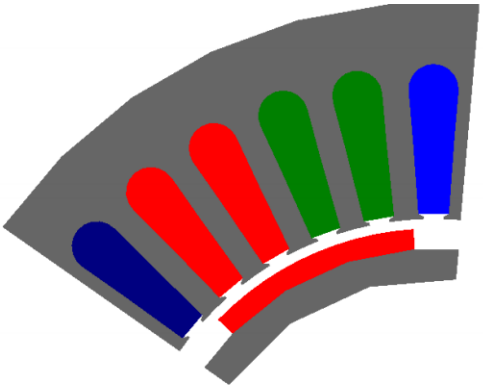

Figure 3.4: Model geometry of FE simulation of PMSG.

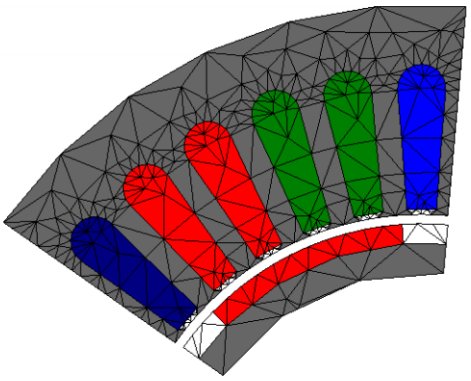

Figure 3.5: Output mesh generated from FE simulation.

tively until the no-load induced voltage is equal to the induced voltage measured from the OCC test. From this, the number of turns is determined as $N_{turns} = 26$. The equation to determine the fill factor of the coils is given by

$$\text{Fill factor} = \frac{\text{Area of copper}}{\text{Area of slot}}. \tag{3.1}$$

The fill factor is assigned in the simulation in order to take into account the voids and insulation between the conductors. To obtain the correct resistance for the simulation the fill factor was chosen as 0.4 and assumed as a general standard ratio.

3.2.2 SEMFEM FE Simulation Results

3.2.2.1 No-load simulation

A no-load test simulation was done. Under no load there are no currents assigned in the dq-axes, the flux generated is solely produced by the permanent magnets. The first simulation was performed under no load conditions without any current excitation, where the dq axis current values were set to zero. The results of the simulation are shown in Fig. 3.6. The waveform of the flux-linkages in each phase is given in Fig. 3.6a where the maximum value of the flux-linkage under no load conditions is 0.36 Wb. From Fig. 3.6a, it can be seen that the stator was correctly aligned since the flux-linkage in phase A is at its maximum value at an electrical position of zero degrees. This is achieved by ensuring that the d-axis is aligned towards the path of the magnetic flux. The resulting flux-linkage in the dq-axis under no load is shown in Fig. 3.6b, where the flux-linkage in the q-axis is zero and a

constant of 0.36 Wb in the d-axis. The result of the cogging torque experienced by the machine at no load is shown in Fig. 3.9a. Here, the electromagnetic torque simulated by SEMFEM is plotted along side the electromagnetic torque calculated in SEMFEM using the torque equation (2.15).

3.2.2.2 Rated-load simulation

For the rated-load simulation, a magnetizing current was assigned only to the q-axis and none assigned to the d-axis. The flux-linkage generated in three-phases of the machine and the dq-axis at rated-load are shown in Fig. 3.7a and 3.7b respectively. The maximum phase current generated at rated load has a maximum amplitude of 6.2 A as shown by the waveforms given in Fig. 3.7a. The current applied in the q-axis is shown in Fig. 3.7b. With a magnetising current only applied in the q-axis and zero currents applied in the d-axis, equation (2.15) from the analytical model becomes

$$T_{mech} = -\frac{3}{2}\left(\frac{p}{2}\right)(\lambda_{pm} i_q), \tag{3.2}$$

where the flux present is due to the permanent magnets since no currents are present in the d-axis. Flux is also generated in the stator which is due to the q-axis current, however no torque is generated from this as the d-axis current is equal to zero. The electromagnetic torque generated by SEMFEM is expected to be relatively constant. The waveform of the output torque simulated is shown in Fig. 3.9b, plotted along with the torque calculated by (3.2), results in an average torque of 8.9 Nm produced. The machine

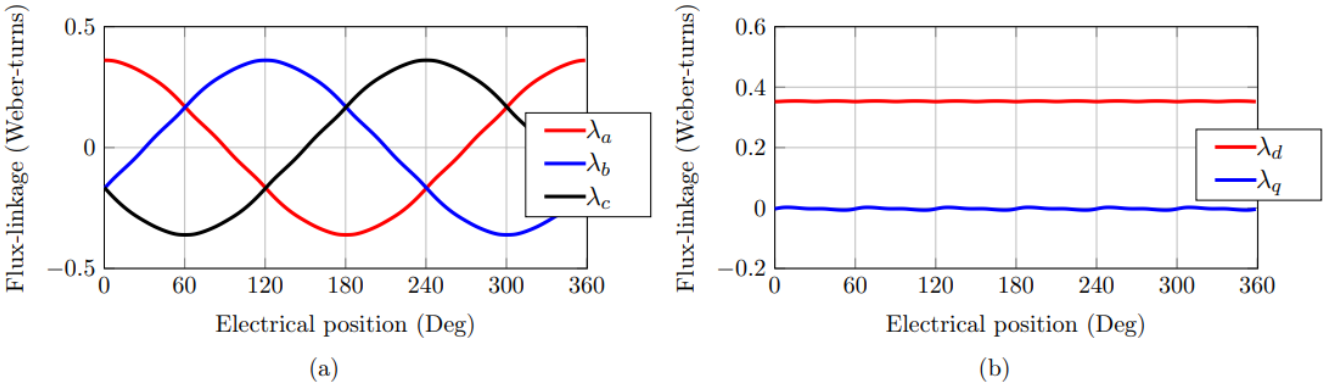

Figure 3.6: (a) Phase flux-linkage versus electrical position results under no load conditionc and (b) dq flux-linkage versus electrical position under no load conditions.

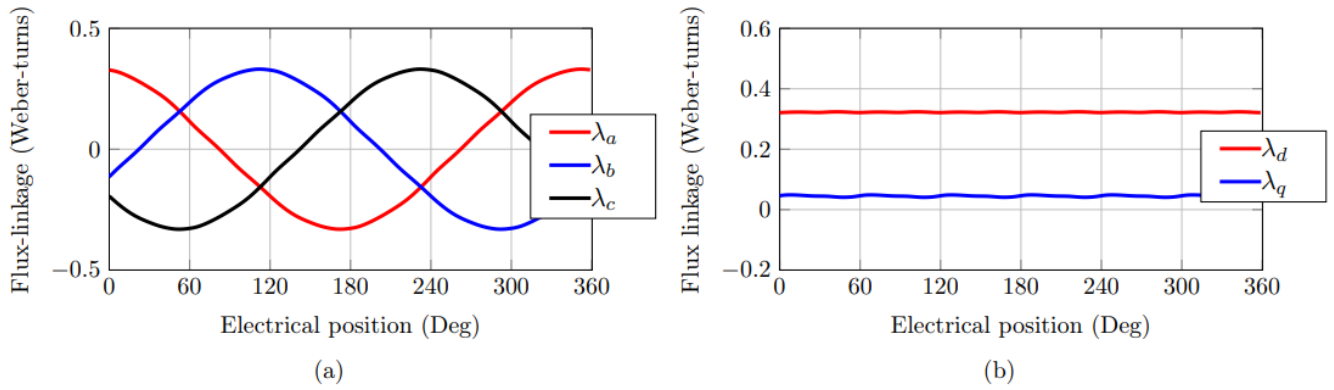

Figure 3.7: (a) Phase flux-linkage versus electrical position results under rated load conditionc and (b) dq flux-linkage versus electrical position under no load conditions.

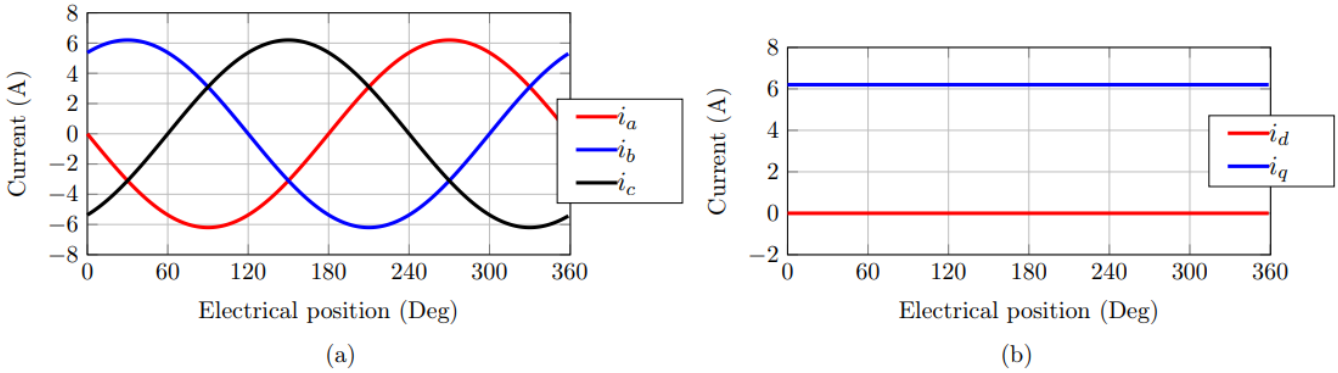

Figure 3.8: (a) Three-phase current versus electrical position at rated load and (b) current in the dq-axis versus electrical position at rated load.

parameters were extracted and determined from the FE analysis performed in SEMFEM. The equations derived in Chapter 2 were used to determine the machine parametrs. The machine parameter determined using SEMFEM FE program are given in Table 3.3.

3.2.3 Machine Modelling in ANSYS Maxwell

To observe the similarities or dissimilarities of the results obtained, and furthermore confirm the accuracy of the results generated, the commercial FEM package ANSYS Maxwell is used to compare the results obtained from SEMFEM. The software package uses a graphical user interface (GUI) to draw the model by using user defined primitives for all the main parts of the machine. The rotor, stator, coil windings and magnets are drawn with the

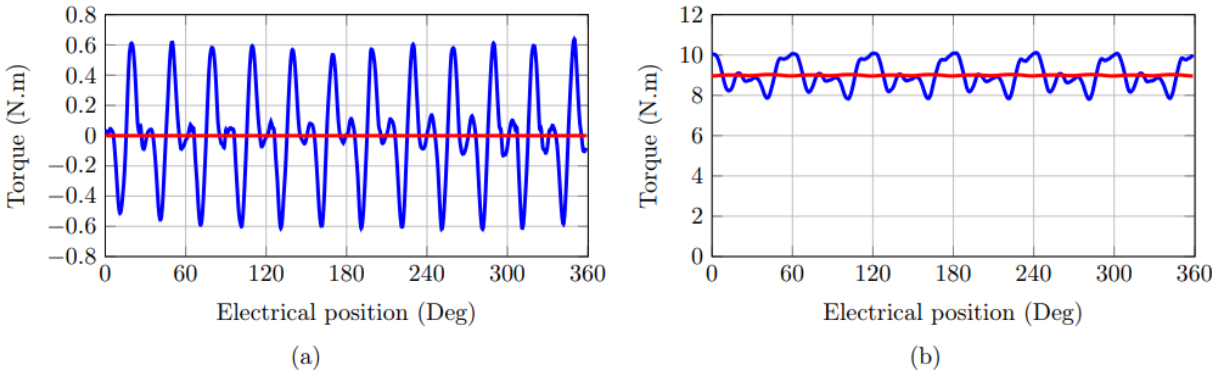

Figure 3.9: (a) No-load torque versus electrical position and (b) rated torque versus electrical position.

Table 3.3: Machine Parameters Determined from Simulation.

Machine Parameter	Value
J	5.2 A/mm^2
R_s	1.135 Ω
L_s	22 mH
λ_{pm}	0.36 Wb
$E_{a(RMS)}$	182.75 V
V_a	153.56 V
I_a	6.2 A
P_{in}	2 491.88 W
P_{out}	2 284.97 W
P_{cu}	122.58 W
P_{core}	82.71 W
η	0.92

same machine dimensions tabulated in Table 3.1. Figure 3.10 shows the 2D cross-sectional drawing of the PM generator modelled in Maxwell. Once the model geometry of the generator is drawn, the material properties are assigned to the stator, rotor, permanent magnets and windings of the machine. Steel laminations of M270-35A were chosen and assigned to the stator and rotor. The permanent magnets material chosen were NdFe30 and copper was assigned for the coil windings. A zero vector potential boundary condition was applied since a full model of the generator was made. Finally dedicated mesh operations were applied to each of the parts of the generator.

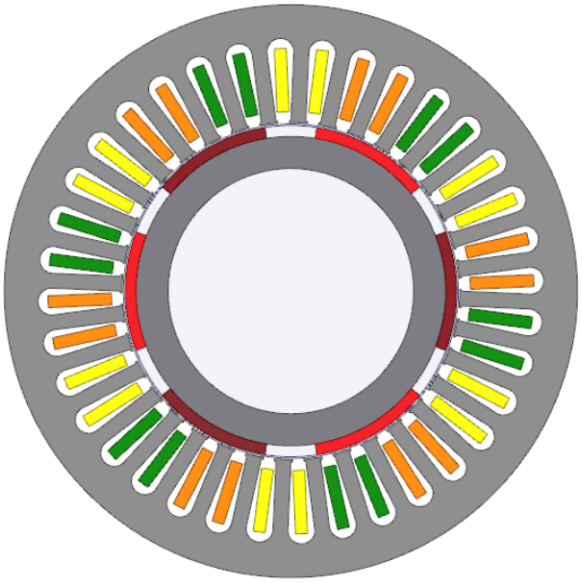

Figure 3.10: Cross-section of PMSG modelled in ANSYS Maxwell.

3.2.4 ANSYS Maxwell Results

A no-load analysis was simulated by computing the fields produced due to the permanent magnets. The resultant flux-linkage generated in each phase from this simulation is shown in Fig. 3.11a having a flux-linkage of approximately 0.5 Wb. The cogging torque of the machine is shown in Fig. 3.11b. For the rated-load simulation, the same sinusoidal phasecurrents generated from SEMFEM were applied to the coils. The resulting the output

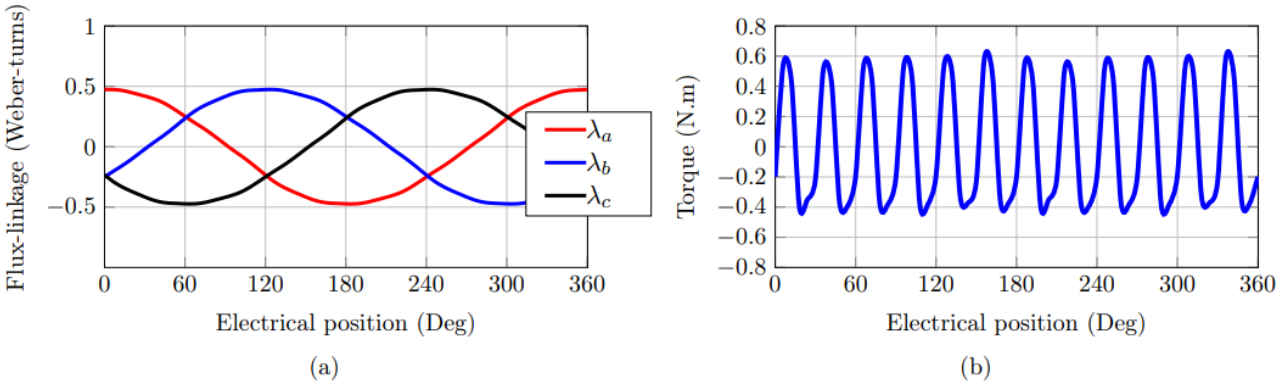

Figure 3.11: (a) Flux-linkage versus electrical position results under no load condi.

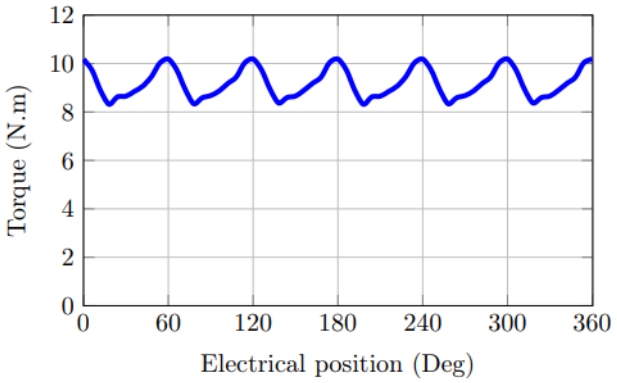

Figure 3.12: Rated torque versus electrical position.

torque waveform is shown in Fig. 3.12 with an average torque value of 9.2 Nm.

3.3 Conclusion

In this Chapter, an FE analysis of a commercial SEW surface mounted PM generator was made. The analysis was conducted using two FEM programs namely SEMFEM and ANSYS Maxwell. The purpose for using the two software was to firstly use the one software (SEMFEM) to extract the machine parameters and then use the other (Maxwell) to evaluate whether the results were correct. The machine was modelled according to the machine dimensions of an existing PM generator. The modelling and simulation results obtained from each software were presented and the machine parameters were determined. From the results obtained from the simulations, it can be seen that results from SEMFEM compare well with those obtained from the commercial FE program Maxwell. A comparison between the results is given in Table 3.4. The modelling of the existing machine was achieved successfully.

Table 3.4: Comparison of SEMFEM and Maxwell Results.

	SEMFEM	Maxwell
λ_{pm}	0.36 Wb-turns	0.5 Wb-turns
Cogging torque (max)	0.63 Nm	0.58 Nm
Torque	8.9 Nm	9.2 Nm

Chapter 4

Alternative Generator Design

In this Chapter an alternative generator is considered. The PM generator is designed as a solution to the problem mention in the problem statement in Section 1.4. In the sections that follow, the generator is designed and modelled using an FE program. The simulation results are presented and discussed. Finally, the machine parameters are determined.

4.1 Motivation

The motivation for this Chapter is to further design an alternative small-scale PM generator that attains a high torque density and low cogging torque.

The full rated turbine speed equals 320 r/min and a rated generator speed of 2240 r/min on the high speed side of a gearbox, with a ratio of 7. From this, the generator frequency at 4, 6 or 8-poles results in 75, 112 or 150 Hz. With a higher generator frequency, the electromagnetic torque developed is subsequently increased [44], which is due to the smaller yoke which creates more space for copper and a larger airgap diameter. Thus, to increase torque density the design of an 8-pole generator is proposed.

A fractional-slot winding configuration is considered. In this slot winding layout, the number of slots across each pole per phase is fractional instead of an integer. This configuration is chosen to provide a smooth torque, which is caused by the reduced periodicity between the poles and slots, and to lower the cogging torque of the machine [45]. The factional slot winding layout considered for the PM generator design is shown in Fig. 4.1.

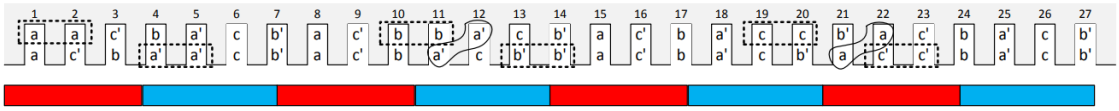

Figure 4.1: Fractional-slot winding layout for 8-poles and 27 slots combination, where the poles are shown by the blocks below and the slots on top.

Unbalanced magnetic pull (UMP) is the total electromagnetic force that acts along the horizontal and vertical axis in the cross-sectional plane of the stator and the rotor and occurs when the axis of the rotor is shifted from the stator axis [46; 47], this is one reason which is specifically for PM motors with no currents. The UMP can also be experienced when the stator current generated radial airgap flux is unbalanced along the circumference of the airgap. Although the (8/27) pole/slot combination is known to cause unbalanced magnetic pull only when stator current is flowing, it will not have a significant impact on the performance of the generator due to the small size of the machine and the low armature reaction effect, which due to the relatively large airgap of the surface mounted machine. The 8/27 combination also has a relatively high winding factor of 0.941. With this taken into consideration, the (8/27) pole/slot combination in this chapter is used solely as an example case to improve the cogging torque and torque density.

Table 4.1: Generator Dimensions.

Machine Parameter	Value
Stator Outer Diameter	105.1 mm
Stator Inner Diameter	61.9 mm
Rotor Diameter	60 mm
Stack Length	120 mm
Number of Slots	27
Number of Poles	8
Air Gap Length	0.5 mm
Number of Winding Layers	2
Coil Span	3

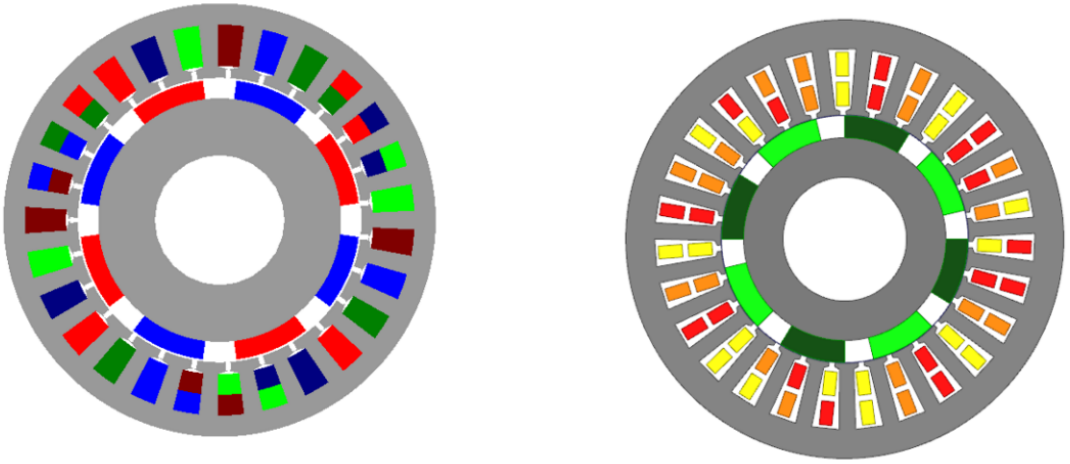

Figure 4.2: Cross section of PM generator modelled in SEMFEM and ANSYS Maxwell respectively.

4.2 Modelling

4.2.1 Machine Specification and Parameters

The PM generator was designed as a 5 kW machine with 8-poles and 27 slots. The machine was designed in SEMFEM and the designed was verified in ANSYS Maxwell. The reason supporting the use of two softwares can be found in Section 3.3. A fractional slot overlap winding was chosen for the stator winding as motivated in the previous section and shown in Fig. 4.1. There are 9 coils in series per phase and 8 coil groups within a phase of which 7 of them have 1 coil and 1 has 2 coils. The machine was designed to have the same volume as the commercial PM generator as in Chapter 3. The stack length of the machine, stator outer diameter, stator inner diameter and rotor outer diameter were kept the same as presented in Table 3.1. The rest of the machine dimensions are given in Table 4.1.

4.2.2 Machine Modelling

The 2-D cross-sectional drawings of the 8-pole PM generator modelled in SEMFEM as well as ANYSYS Maxwell are shown in Fig. 4.2. Due to the fractional-slot winding of the stator, a double winding layer is used for the simulation. The coil span required for the stator winding is 3. The model geometry is drawn in SEMFEM using the pole pitch and the slot pitch to effectively draw the stator and rotor of the machine. The pole pitch and slot pitch are calculated by the equations given by

$$\text{pole pitch} = \frac{360^o}{p} \tag{4.1}$$

$$\text{slot pitch} = \frac{360^o}{Q}, \tag{4.2}$$

where p is the number of poles and Q is the number of slots. Due to the asymmetrical nature of the machine winding layout, the whole machine is drawn for the FE analysis. The input current required for the design is determined from the current density. The current density typically ranges between 5-7 A/mm^2. A typical current density of J = 6 A/mm^2 was chosen and applied to the simulation. The phase current can be determined by

$$J = \frac{NI_{phase}(RMS)}{A_s k_f}, \tag{4.3}$$

where J is the RMS current density, N is the number of turns per slot, $I_{phase(RMS)}$ is the phase current, As is the area of the stator and k_f is the fill factor. For the design of this machine, a standard ratio of 0.4 was assumed as the fill factor. The N number of turns per coil for the design is $N_{turns} = 170$ which is determined in Section 4.3. The same approach described in Sections 3.2.1 and 3.2.3 was followed to model and analyse the PM generator in SEMFEM and Maxwell.

4.3 Simulation Procedure

To have the generator running at unity power factor, where the current of the generator is in phase with the terminal voltage, the following procedure was followed in the static FEA simulation as adopted from [48]. Here, the load angle Δ and the current angle α are equal resulting in a power factor angle θ that is equal to zero. The same procedure was followed for the static FEA simulation in Chapter 3.

The power factor angle θ is given by

$$\theta = \Delta - \alpha. \tag{4.4}$$

In general, it is accepted that $L_q = L_d$ with the use of surface mounted PMs, however this does not hold when the current angle α is zero. In this case L_q and L_d are determined by

$$\begin{aligned} L_q &= \frac{\lambda_q}{-I_q} \\ L_d &= \frac{\lambda_d - \lambda_{pm}}{-I_d}. \end{aligned} \tag{4.5}$$

The dq-voltage and currents are related to each other by the following,

$$\begin{aligned} V_q &= \sqrt{2} V_{rms} \cos(\Delta), \\ V_d &= \sqrt{2} V_{rms} \sin(\Delta). \end{aligned} \tag{4.6}$$

$$\begin{aligned} I_q &= \sqrt{2} I_{rms} \cos(\alpha), \\ I_d &= \sqrt{2} I_{rms} \sin(\alpha). \end{aligned} \tag{4.7}$$

$$V_q^2 + V_d^2 = 2V_{rms}^2. \tag{4.8}$$

$$I_q^2 + I_d^2 = 2I_{rms}^2. \tag{4.9}$$

where V_{rms} is RMS voltage of the AC equivalent of the rectifier-DC-DC converter-battery load voltage which is given by

$$V_{bat} = \frac{\sqrt{2}(V_{dc} + 2V_{diode})}{\pi}, \tag{4.10}$$

where $V_{dc} = V_{bat}/D$ is the input of the DC-DC converter. V_{bat} is the battery voltage which forms the output of the DC-DC converter and V_{diode} is the voltage drop across the diode.

The RMS values of (4.5) and (4.6) are substituted into the dq-equations of (2.14) in order to rewrite the dq voltage and current values in terms of their RMS values. Thereafter, the dq-equations (2.14) are rewritten with I_{rms} as the subject of the equation, which gives

$$I_{rms} = \frac{\sqrt{2} V_{rms} \cos(\alpha) - \omega_e \lambda_{PM}}{\sqrt{2}(-R_s \cos(\alpha) - \omega_e L_q \sin(\alpha))}. \tag{4.11}$$

$$I_{rms} = \frac{\sqrt{2} V_{rms} \sin(\alpha)}{\sqrt{2}(-R_s \sin(\alpha) + \omega_e L_d \cos(\alpha))}. \tag{4.12}$$

Equations (4.10) and (4.11) are then used to solve for the unknown terms I_{rms} and α numerically.

To calculate and have the generator running at unity power factor, the following iterative procedure is conducted:

1. At cut-in speed there is zero generator current flowing, resulting in the dq-equations of (2.14) being reduced to $V_q = \omega_e \lambda_{pm}$ and $V_d = 0$. With ω_e known, N_{turns} is calculated to produce the required λ_{pm} value to achieve the voltage at the cut-in speed.

2. To obtain the initial λ_{pm}, the SEMFEM FE simulation is run with I_{rms} and α equal to zero. With this, the number of turns per phase N_{turns} is determined and set.

3. The first iteration is run. Here, I_{rms} is equal to the allowed current density of $J = 6A/mm^2$. The value of $\hat{\mathrm{I}} \pm is then set to zero at the rated turbine speed. With this in place, the dq-currents become \mathrm{I}_d = 0$ and $I_q = \sqrt{2} I_{rms}$.

4. After the first iteration, the value of L_q is determined by $L_q = \lambda_{pm}/I_q$. At this instance it is assumed that $L_q = L_d$.

5. For unity power factor, the current angle is equal to the load angle. The V_{rms} voltage which is at the diode rectifier is calculated using (4.9), which is done for a 48 V battery bank connected to a DC-DC converter. By knowing that the angle α is between 0^o and 90^o, equations (4.10) and (4.11) are then solved simultaneously in order to calculate the values of I_{rms} and α.

6. The new values that are calculated for I_{rms} and α are then set.

7. The current density J is calculated from the new values and then used in the proceding iteration.

8. The second iteration is run. Here, L_q and L_d are determined from (4.4) since the assumption that $L_q = L_d$ is now invalid.

9. A third iteration is then performed, and is done with the new calculated values for I_{rms} and α.

From the procedure followed, three FE iterations from the simulation are necessary for the current I_{rms} to converge accurately.

4.4 FE Simulation Results

The simulation results were obtained from the FE analysis done in SEMFEM and Maxwell. The first set of results are obtained from SEMFEM under the rated q-axis current condition. The results of the flux-linkage obtained from the simulation are shown in Fig. 4.3a, where the flux-linkage per phase is plotted versus the electrical position and results in a generator PM flux-linkage of 0.226 Wb-turns. The cogging torque is shown in Fig. 4.4a having a peak torque amplitude of 0.4 Nm for the SEMFEM simulation. The output torque developed from the PM generator design is presented in Fig. 4.5a, where the average torque obtained is 19.05 Nm. The second set of results are those obtained from Maxwell which were also analysed under rated q-axis conditions. The generated flux-linkage per phase is shown in Fig. 4.3b. The waveform showing the cogging torque is shown in Fig. 4.4b. An output torque of 19.014 Nm developed as shown in Fig. 4.5b.

The machine parameters were determined by following the approach discussed in section 3.2. The machine parameters determined for this PM generator design are given in Table 4.2.

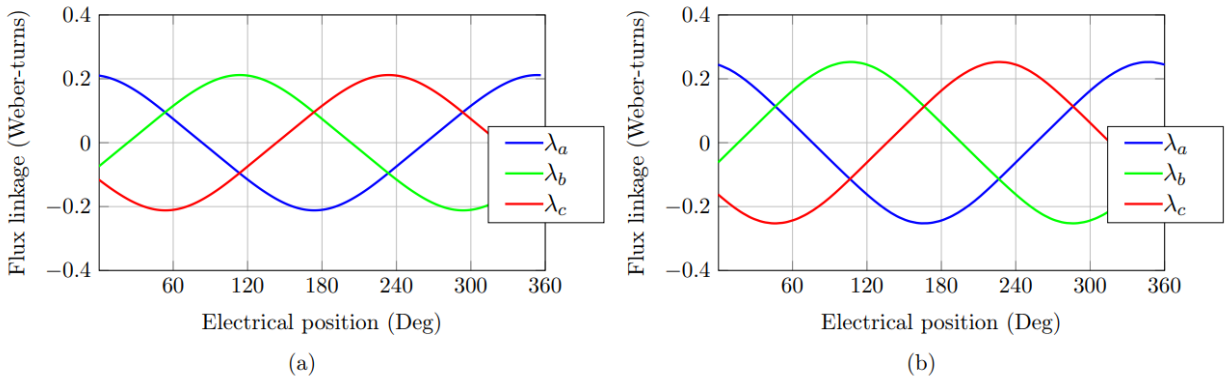

Figure 4.3: Phase flux-linkage versus electrical position at rated load simulated by (a) SEMFEM and (b) Maxwell.

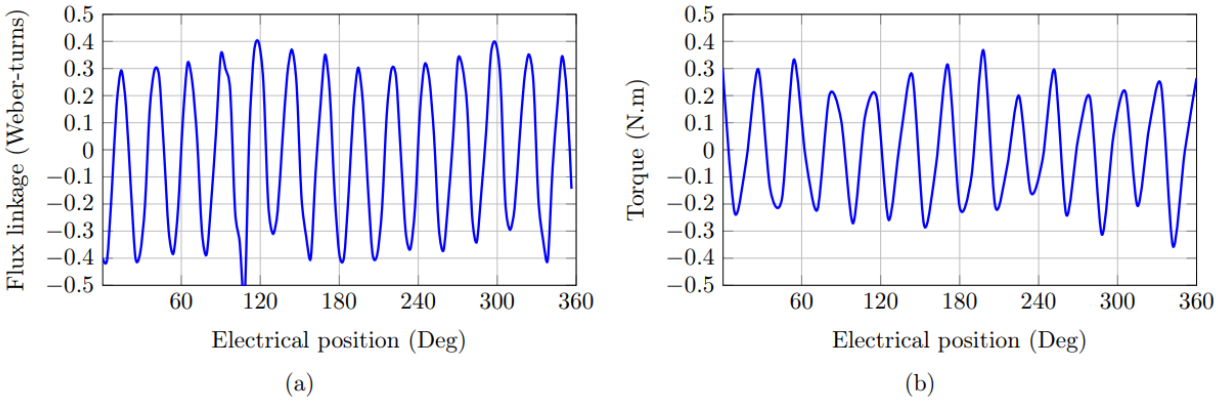

Figure 4.4: Cogging torque versus electrical pposition at no-load simulated by (a) SEMFEM and (b) Maxwell.

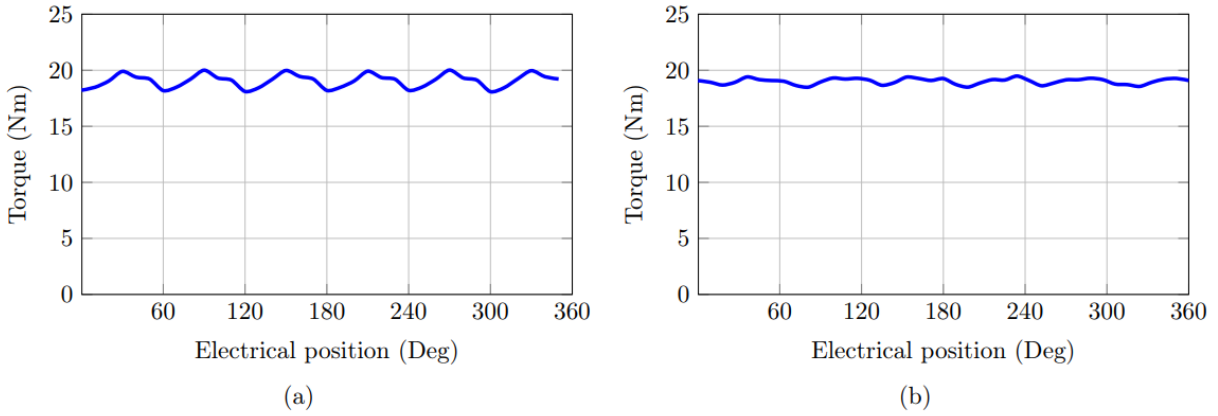

Figure 4.5: Output torque versus electrical pposition at rated load simulated by (a) SEMFEM and (b) Maxwell.

Table 4.2: Machine Parameters Determined from Simulation.

Machine Parameter	Value	Machine Parameter	Value
J	6 A/mm^2	I_a	8.48 A
R_s	3.02 Ω	P_{in}	4 645.64 W
L_s	5.71 mH	P_{out}	3 936.6 W
λ_{pm}	0.226 V.s	P_{cu}	594.4 W
$E_{a(RMS)}$	191.44 V	P_{core}	114.64 W
V_a	162 V	η	0.85

4.5 Conclusion

In this Chapter an alternative PM generator was designed and evaluated. The PM generator was designed to achieve a high torque density and low cogging torque by increasing

the number of poles and changing the slot/pole combination. The generator was designed in SEMFEM and ANSYS Maxwell. The results obtained from both simulations compared well. The design approach was explained and executed. The FE analysis showed that an output torque of 19.05 Nm was generated. The cogging torque of the PM generator was found to have a maximum of 0.4 Nm from the SEMFEM simulation. From the machine design, the output torque is increased and the cogging torque has decreased but by a very small margin of 0.2 Nm. Table 4.3 gives a comparison between the 6-pole PM generator of Chapter 3 and the 8-pole PM generator in this chapter. The motives behind the design of this alternative PM generator were implemented and achieved.

Table 4.3: Comparison of SEMFEM and Maxwell Results.

Machine Parameter	6-Pole PM Generator	8-Pole PM Generator
Cogging torque (Nm)	0.63	0.4
Rated torque (Nm)	8.9	19.05
Rated torque ripple (%)	23.65	10.08

Chapter 5

Maximum Power Point Tracking Control

In this chapter, a simple control method is proposed to achieve MPPT for wind energy systems that are DC-grid connected.

A brief description of the system is given, the steady state analysis of the wind energy system is made, the control method proposed is discribed and explained. Lastly, the stability of the system in response to fluctuations in the wind speed is further investigated.

The power losses of the PMSG, as considered in Chapter 2, are not modelled in the same manner in this Chapter. In this Chapter, the losses are rather lumped together as rotational losses on the high speed side of the gearbox by equation (5.2).

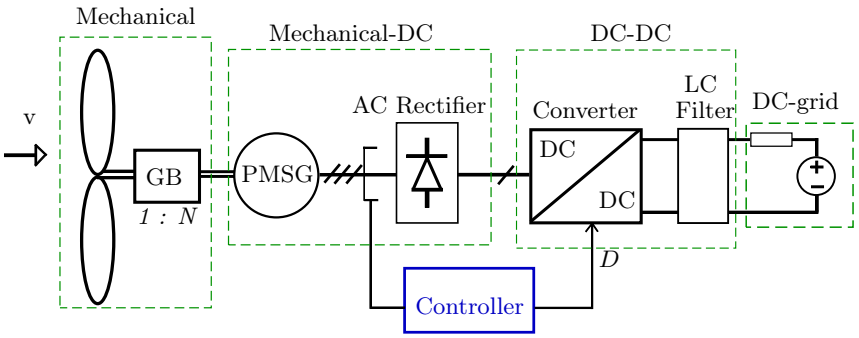

Figure 5.1: Layout of PM wind generator system connected to a DC-grid.

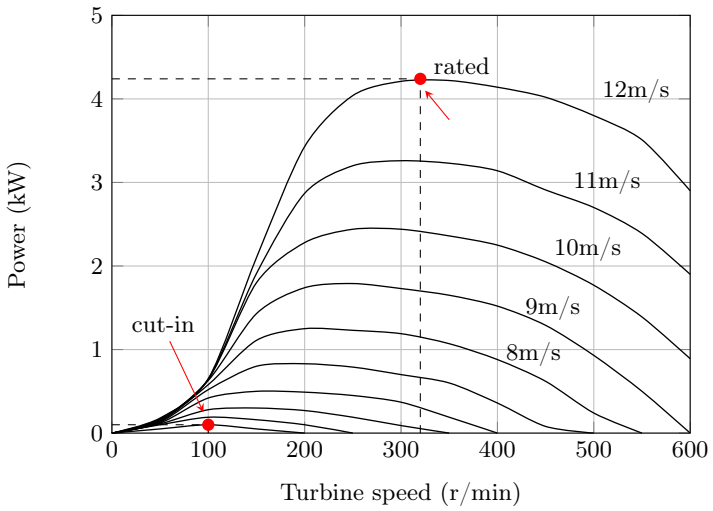

Figure 5.2: Wind turbine power versus turbine speed with wind speed a parameter.

5.1 System Description

The wind energy system considered for the study of the proposed control method is shown in Fig. 5.1. The system consists of a wind turbine that has fixed-pitch blades, and is connected to a planetary gearbox having a ratio of 1:7. The power-speed characteristic curve of this wind turbine is shown in Fig. 5.2. It can be noted that these power-speed characteristics of the wind turbine blades can nowadays easily and accurately attained from the blade element method or computational fluid dynamics analysis. The cut-in speed of the turbine is at 100 r/min. The rated operating point of the turbines maximum power is at a wind speed of 12 m/s, which correlates to a rated power of 4.2 kW and a turbine speed of 320 r/min. Both operating points are shown in Fig. 5.2. The surface mounted permanent magnet synchronous generator (PMSG) is mechanically connected to the gearbox and electrically connected to a 3-phase full-bridge diode rectifier. The PMSG is a 3-phase, 8-pole generator. The diode rectifier is connected to a step down Buck DC-DC converter, which is then connected to the DC-grid via an LC filter. The filter is designed to have a 10 kHz switching frequency. The filter is also designed to have a low average boundary current between continous and discontinuous conduction of less than 1 A. The DC-grid voltage of the system is 48 V. The design parameters and specifications of the system can be found in Table 5.1.

Table 5.1: WECS PARAMETERS

Wind turbine & Gearbox	
Turbine inertia, J_t (kg·m^2)	21
Mechanical damping coefficient, B (N·m·s/rad)	0.007
Gear ratio, N	1:7
Mechanical time constant, τ_m (s)	61.22
Permanent Magnet Synchronous Generator	
Stator phase resistance, R_s (Ω)	3.024
Armature inductance, L_s (mH)	5.7
Generator PM flux linkage per pole, λ_m (V.s)	0.226
Electrical time constant, τ_e (ms)	2.142
DC - DC Converter	
Input voltage, V_{in} (V)	101-260
Rated output current, I_{out} (A)	87.5
Switching frequency, f_s (kHz)	10
LC filter	
Inductance, L_f (mH)	3
Resistance, R_f (Ω)	0.02
Capacitance, C_f (μF)	200
DC-Grid	
DC-grid voltage, V_i (V)	48
Internal resistance, R_i (Ω)	0.01

5.2 Steady State System Analysis

In this section the steady-state calculations of the system are established and an equation to calculate the duty cycle value to have the system at MPPT is determined.

5.2.1 Turbine, gearbox and PMSG

It is possible to determine the turbine power P_t that occurs at a specific wind speed v and rotational speed ω_t from the turbine power curves. This power is expressed as

$$P_t = \omega_t \tau_t, \tag{5.1}$$

where τ_t is the torque of the turbine. The rotational losses P_{rot} are made up of the gearbox losses, the friction and windage losses and core losses of the PMSG combined. The rotational losses are modelled on the high speed side of the gearbox as

$$P_{rot} = B\omega_g^2, \tag{5.2}$$

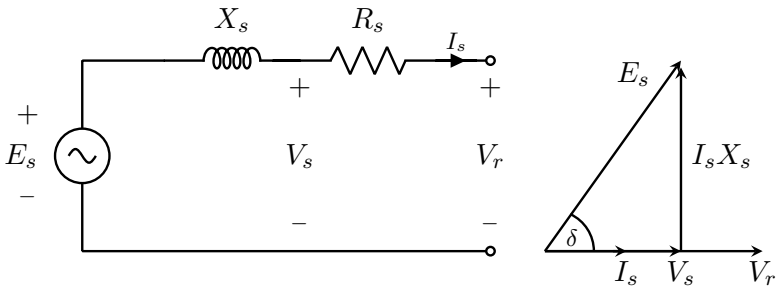

Figure 5.3: Per phase equivalent circuit and phasor diagram of PMSG.

at a speed of $\omega_g = N\omega_t$, where N is the gearbox ratio. In (5.2), B is the mechanical damping coefficient of the system. B is estimated based on analytical loss calculations and is given in Table 5.1. The input power of the generator which is mechanically developed is given by the equation

$$P_g = \omega_g \tau_g = P_t - P_{rot}, \tag{5.3}$$

where τ_g is the generator torque. The power of the generator is then modelled electrically according to the lossless part of the per phase equivalent circuit of the PMSG, which is shown in Fig. 5.3, and thus given as

$$P_g = \frac{3V_s E_s \sin(\delta)}{X_s}, \tag{5.4}$$

In (5.4) $X_s = \omega_e L_s$ and $E_s = \omega_e \lambda_m / \sqrt{2}$ where ω_e is the electrical speed and λ_m is the generator's PM flux linkage per pole given in Table 5.1. It is assumed that the PMSG is operating at unity power factor with respect to its fundamental component of the voltage and the current with the diode rectifier as a load. This is shown by the phasor diagram in

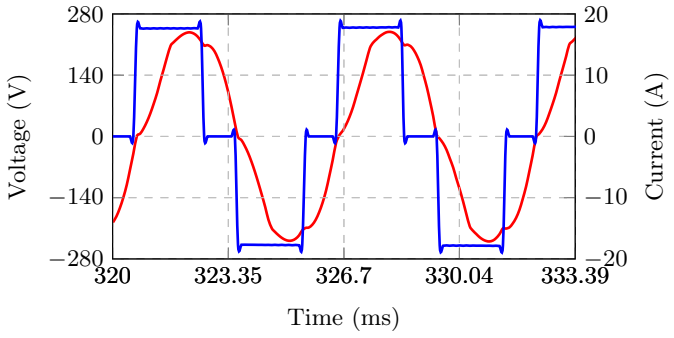

Figure 5.4: PMSG's terminal line voltage and phase current at diode rectifier input.

Fig. 5.3. Under such operation the voltage V_s is given as

$$V_s = E_s \cos(\delta), \tag{5.5}$$

and as a result (5.4) can be simplified as

$$P_g = \frac{3E_s^2 \sin(2\delta)}{2X_s}. \tag{5.6}$$

The power angle δ, shown in Fig. 5.3, can be determined from (5.6) with P_g, E_s and X_s known as

$$\delta = \frac{1}{2}\sin^{-1}(\frac{2P_g X_s}{3E_s^2}). \tag{5.7}$$

From (5.7), the power angle can be determined. With δ known, the voltage V_s and the generator current I_s can be calculated. The voltage V_s is determined from equation (5.5) and I_s can be determined in the following ways

$$I_s = \frac{P_g}{3V_s} = \frac{P_g}{3E_s \cos(\delta)} = \frac{E_s \sin(\delta)}{X_s}. \tag{5.8}$$

Lastly the output power and the output voltage of the generator located at the input terminals of the full-bridge diode rectifier can be determined using the per phase equivalent circuit of the generator in Fig. 5.3 by the following

$$\begin{aligned} P_r &= 3V_r I_s \\ V_r &= V_s - I_s R_s. \end{aligned} \tag{5.9}$$

5.2.2 Rectifier and DC-DC Converter

For the purpose of simplifying the analysis, the diode rectifier and the DC-DC converter are considered to be lossless. In Fig. 5.4 the waveforms of the PMSG's terminal line voltage and phase current at the input of the diode rectifier are shown. It is seen that the voltage at the terminals of the rectifier are in the form of quasi-square waves as shown in Fig 5.4. The generator's output voltage V_r from (5.9) is the RMS value of the fundamental component of the quasi-square terminal voltage. With V_r known from (5.9) and as it is derived by [24], the rectified DC voltage is determined as

$$V_d = \frac{\pi}{\sqrt{2}} V_r. \tag{5.10}$$

With the assumed sinusoidal input line currents as shown in Fig. 5.4, the average of the rectified DC current, according to [24], is calculated as

$$I_d = \frac{3\sqrt{2}}{\pi} I_s = 1.35 I_s. \tag{5.11}$$

Furthermore, the DC power can be calculated from

$$P_d = V_d I_d = 3 V_r I_s = P_r. \tag{5.12}$$

Taking into consideration that the DC-DC converter is a buck converter its output voltage becomes $V_o = DV_d$ and its output current is $I_o = I_d/D$, where D is the switching duty cycle. The DC-grid is modelled as a voltage source V_i in series with a resistor R_i as shown in Fig. 5.1. From this, the output voltage of the DC-DC converter can be re-written as

$$V_o = DV_d = I_o R_e + V_i = \frac{I_d}{D} R_e + V_i. \tag{5.13}$$

where $R_e = R_f + R_i$, where R_f is the resistance of the filter inductor and R_i is the DC-grid internal resistance, and V_i is the DC-grid voltage. Finally the duty cycle D can then be solved by simplifying (5.13) as

$$\begin{aligned} 0 &= V_d D^2 - V_i D - I_d R_e \\ \Rightarrow D &= \frac{V_i + \sqrt{V_i^2 + 4 V_d I_d R_e}}{2 V_d}. \end{aligned} \tag{5.14}$$

The above duty cycle calculation shows that if the turbine speed (or else the generator speed or frequency) and the maximum power of the turbine at that speed are known, then the duty cycle can be determined to have the system at MPPT. Note that if the DC-grid voltage varies then the duty cycle calculation takes this into account by (5.14).

5.3 Feedforward Control

In this section the control method used to have the turbine operating at its maximum operating point is described and explained. The analysis and application of equations (5.1) to (5.14) results in a unique duty cycle for each given steady state turbine power and turbine speed. Hence, if we consider the maximum turbine power operating points and thus the maximum power point turbine and generator speed, a unique optimum duty

cycle that is a function of the generator speed/frequency, can be determined by means of (5.14). Therefore by measuring the generator frequency to determine the appropriate duty cycle value according to the optimum duty cycle function, the DC-DC converter is then able to control the system so that the turbine is able to slide along its maximum power point trajectory as the wind speed changes. Alternatively, the DC-link voltage V_d of (5.10) can be measured instead of measuring the generator frequency in order to determine the optimum duty cycle as a function of the voltage V_d.

5.3.1 Duty Cycle Function

The optimum duty cycle function is investigated by applying (5.1) to (5.14) to the wind generator system as described in section 5.2. The equations were calculated at each of the maximum turbine power operating points at the corresponding generator speed. The results of the calculation for the system is shown in Fig. 5.5, where the optimum duty cycle function is plotted against the generator frequency. A second duty cycle function was determined in order to determine the effect that the losses have on the optimum duty cycle. This was determined by ignoring all the losses in (5.1) to (5.14). The plot of this second function is also shown in Fig. 5.5. From this figure it can be seen that the losses in the system make relatively little difference in the optimum duty cycle function. The calculations using (5.1) to (5.14) clearly show that the duty cycle function can be determined in a simple approach, furthermore it is clear that the system may be taken as

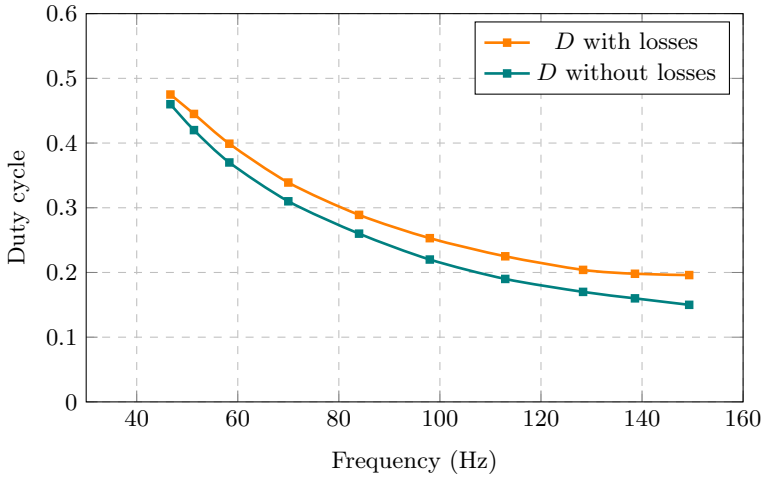

Figure 5.5: Optimum duty cycle function calculated with and without losses.

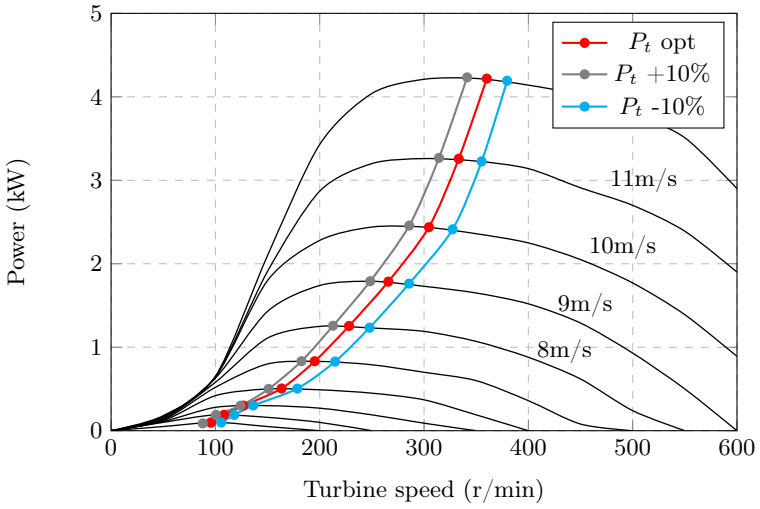

Figure 5.6: Simulated steady state operating turbine power versus turbine speed with ± 10 % errors in the optimum duty cycle function.

lossless. It must be noted that the losses of the system are the only real parameters that can change with a change in temperature. This contributes to the robustness of the system. To investigate the accuracy of the MPPT achieved using the determined optimum duty cycle function of Fig. 5.5, the latter was implemented in a Matlab Simulink simulation of the entire system. The steady state operating power point results of this simulation are shown in Fig. 5.6, labelled as Pt opt on the graph. From this graph it can be seen that the system accurately tracks the maximum power point of the turbine as the wind speed changes.

5.3.2 Sensitivity to D and V_i

It is a question on how sensitive the proposed duty cycle feedforward control is to firstly errors in the duty cycle function and secondly to variations in the DC-grid voltage Vi. This was investigated by introducing ±10% errors to the optimum duty cycle function as shown in Fig. 5.5 and implemented int he Simulink simulation of the system. The results of how the effects of the errors introduced have on the power point tracking of the turbine are shown in Fig. 5.6. From this it is clear that the system is very insensitive to relatively large errors in the duty cycle function.

Furthermore, the DC grid voltage Vi was varied by 0.1 pu according to general grid code regulations. The simulated results of this variation on the operating turbine power

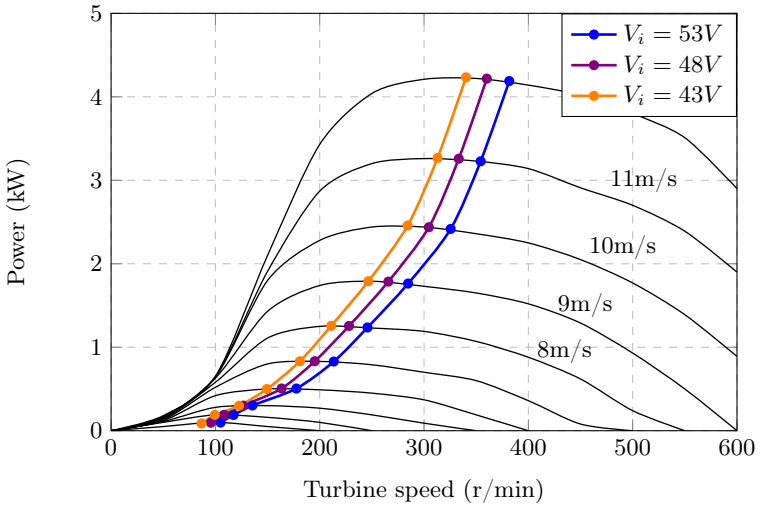

Figure 5.7: Simulated steady state operating turbine power versus turbine speed with ± 0.1 pu dc-grid voltage variation.

points are shown in Fig. 5.7. The small error in the maximum power extracted shows that the proposed control is also insensitive to ±10% DC-grid voltage variations.

5.4 Dynamic System Analysis

In this section the dynamics of the proposed wind energy system are investigated. This is to determine whether the system is stable or not. To achieve this, we replaced the AC generator and the full bridge diode rectifier with an equivalent DC generator that is mechanically connected to the turbine-gearbox on the one side and connected to the DC link between the rectifier and the step-down converter. Furthermore, the low voltage electrical side of the step-down converter is referred to the high voltage DC-link side. Doing so results in a combined DC equivalent electrical model as shown in Fig. 5.8. This model can be used to derive a tranfer function of the system.

5.4.1 Turbine and Gearbox System

To model the dynamics of the turbine and gearbox, the system is considered on the high speed side of the gearbox as

$$T_t^{'} - T_g = J_t^{'} \frac{d\omega_g}{dt} + B\omega_g. \tag{5.15}$$

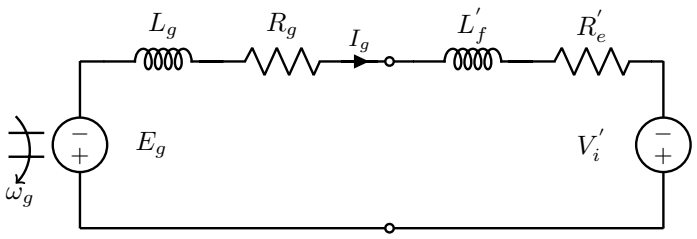

Figure 5.8: Equivalent DC model of PM generator and DC link load.

Here B represents the damping coefficient of the system due to the friction and windage, gearbox and core losses of the system on the high speed side of the gearbox. The superscript (') denotes the high speed side of the gearbox. In equation (5.15), only the turbine inertia is considered since is much larger than the other system inertias.

5.4.2 DC equivalent PM generator

Deriving an equivalent DC generator model requires that the equivalent model has the same losses, open and short circuit characteristics and the same time constant as the actual DC rectified generator system. To have the conductor losses the same for both models, then

$$3I_s^2 R_s = I_g^2 R_g, \tag{5.16}$$

where I_g and R_g are the DC generator current and resistance respectively. To have the diode rectified system the same for both models, the relationship between I_s and I_g can be found from (5.11), as a result R_g can be calculated as

$$R_g = \frac{\pi^2}{6} R_s. \tag{5.17}$$

To have the L/R time constant the same for both models, it follows from (5.17) that

$$L_g = \frac{\pi^2}{6} L_s. \tag{5.18}$$

The open circuit DC voltages of the equivalent model and the actual model should also be the same, therefore from the voltage equation of (5.10) and by using (5.5) and (5.9) at no-load, the DC generator's open circuit voltage and thus the back EMF, E_g can be

expressed as

$$\begin{aligned} E_g &= \frac{\pi}{\sqrt{2}} E_s \cos(\delta) \\ &= \left(\frac{\pi}{\sqrt{2}} \frac{\lambda_m}{\sqrt{2}} \frac{p}{2} \cos(\delta) \right) \omega_g \\ &= K_g \omega_g, \end{aligned} \tag{5.19}$$

where p is the number of poles. The power angle δ in (5.19) is a variable, meaning that K_g varies with the load making it quite difficult to use. However, since δ is relatively small ($\delta \angle 15^o$) for surface mount PM generators up to full load so that $\cos(\delta)$ is averagely approximated as $\cos(\delta) \approx 0.98$, and thus K_g from (5.19) can be approximated as

$$K_g \approx \left(\frac{0.98\pi}{4} \right) p\lambda_m = 0.77 p\lambda_m. \tag{5.20}$$

Finally as a result from the above, the dynamic voltage equation of the equivalent DC generator results as the following

$$e_g = v_g + i_g R_g + L_g \frac{di_g}{dt}, \tag{5.21}$$

where

$$e_g = K_g \omega_g \text{ and } T_g = K_g i_g. \tag{5.22}$$

5.4.3 DC link equivalent load

The equation governing the dynamics of the low-voltage-circuit-side of the step-down converter is described as

$$v_o = v_i + i_o R_e + L_f \frac{di_o}{dt}, \tag{5.23}$$

where $R_e = R_f + R_i$, which are respectively the filter resistance and the internal source resistance. It must be noted that the lower case letters in (5.23) are used to indicate the dynamics of the average (not the high switching frequency) output converter and DC-grid voltages and output current of the circuit. In equation (5.23), the filter capacitor is ignored for the purpose of simplicity since it has negligible effect, but still incorporated into the modelling of the system. The circuit can be referred to the high voltage DC-link side of the converter by dividing throughout equation (5.23) by the duty cycle D, which results

in the following

$$\begin{aligned} \frac{v_o}{D} &= \frac{v_i}{D} + i_o D\left(\frac{R_e}{D^2}\right) + \left(\frac{L_f}{D^2}\right)\frac{di_o D}{dt} \\ \Rightarrow v_g &= v_i^{'} + i_g R_e^{'} + L_f^{'}\frac{di_g}{dt}. \end{aligned} \tag{5.24}$$

It is important to note that the duty cycle is considered to be constant for the moment in the dynamics. It can also be noted that the voltage v_g and the current i_g in (5.23) are the voltage and current of the DC generator of (5.21) respectively. From (5.21) and (5.23), the equivalent model of the electrical system can be determined as

$$\begin{aligned} e_g &= v_i^{'} + i_g(R_g + R_e^{'}) + (L_g + L_f^{'})\frac{di_g}{dt} \\ &= v_i^{'} + i_g R_d + L_d\frac{di_g}{dt}. \end{aligned} \tag{5.25}$$

The DC equivalent electrical circuit model of equation (5.25) is shown in Fig. 5.8. The electrical time constant of the system can be determined from the circuit as

$$\tau_e = \frac{L_d}{R_d} = \frac{L_g + L_f^{'}}{R_g + R_e^{'}} = \frac{D^2 L_g + L_f}{D^2 R_g + R_e}, \tag{5.26}$$

and it is shown to be a function of the duty cycle.

5.4.4 Transfer function derivation

Following that the dynamic model has been explained and described in Subsections 5.4.1 - 5.4.3, the transfer function can now be derived. The transfer function of the mechanical part of the system is determined from (5.15) as

$$\frac{\omega_g(s)}{T_t^{'}(s) - T_g(s)} = \frac{1}{B(1 + s\frac{J_t^{'}}{B})} = \frac{1}{B(1 + s\tau_m)}, \tag{5.27}$$

where τ_m is the mechanical time constant of the system. The value of the τ_m can be found in Table 5.1. The transfer function of the electrical part of the system is determined from (5.25) and is given as

$$\frac{i_g(s)}{e_g(s) - v_i^{'}(s)} = \frac{1}{R_d(1 + s\frac{L_d}{R_d})} = \frac{1}{R_d(1 + s\tau_e)}, \tag{5.28}$$

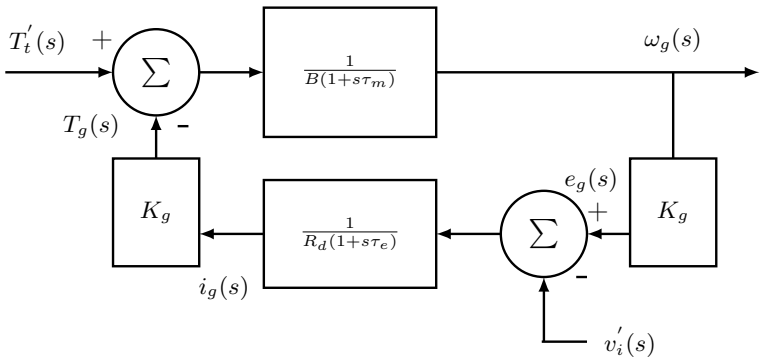

Figure 5.9: Transfer function block diagram between input torque and output generator speed.

where τ_e is the electrical time constant of the system as given in Table 5.1. Note that in equations (5.27) and (5.28), according to (5.22), $T_g(s)$ and $e_g(s)$ become

$$T_g(s) = K_g i_g(s) \text{ and } e_g(s) = K_g \omega_g(s). \tag{5.29}$$

The block diagram depicting the transfer function of equation (5.27) to (5.29) is shown in Fig. 5.9. From this a closed-loop transfer funciton between the input torque and output generator speed is detemined as

$$\frac{\omega_g(s)}{T_t'(s)} = \frac{R_d(1+s\tau_e)}{BR_d(1+s\tau_m)(1+s\tau_e)+K_g^2}. \tag{5.30}$$

Since the electrical time constant is very small as compared to the mechanical time constant, we neglect it and equation (5.30) becomes

$$\begin{aligned} \frac{\omega_g(s)}{T_t'(s)} &\approx \frac{R_d}{BR_d(1+s\tau_m)+K_g^2} \quad [\tau_e \ll \tau_m] \\ &= \frac{R_d}{BR_d+K_g^2}.\frac{1}{1+s\tau_m'}, \end{aligned} \tag{5.31}$$

where

$$\tau_m' = \frac{BR_d}{BR_d+K_g^2}\tau_m. \tag{5.32}$$

The approximate transfer function of the system can be determined according to (5.31), using the system parameters given in Table 5.1 and by selecting a duty cycle value of

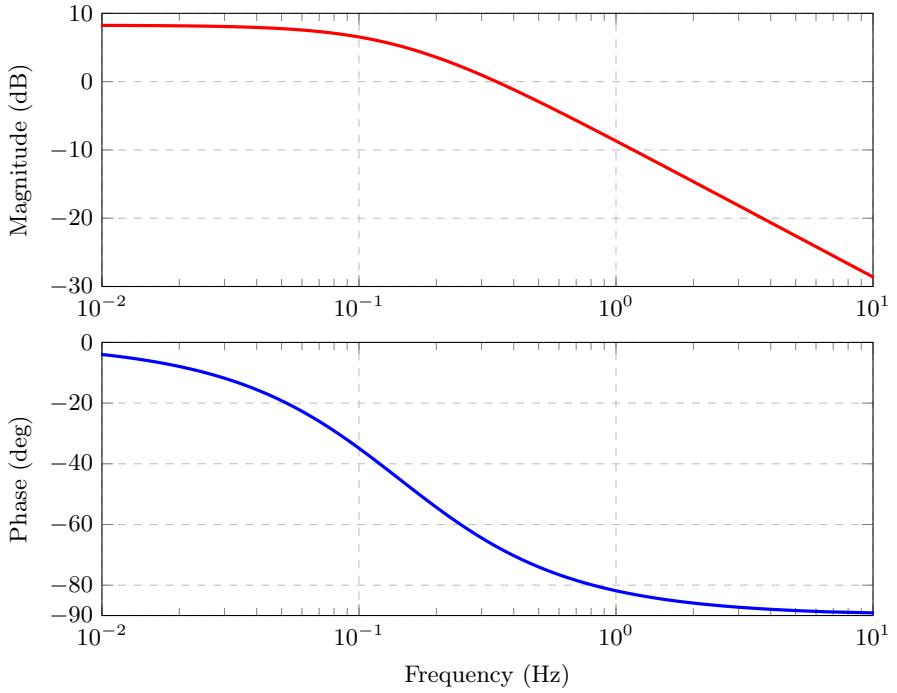

Figure 5.10: Bode plot of the transfer function of the complete system.

$D = 0.5$, the following transfer function was obtained

$$\begin{aligned} \frac{\omega_g(s)}{T_t'(s)} &\approx \frac{R_d}{BR_d + K_g^2} \cdot \frac{1}{1 + s\tau_m'} \\ &= 2.6 \frac{1}{1 + 1.11s}. \end{aligned} \tag{5.33}$$

From (5.31) it can be seen that the system is a dominant first order system and acts as a low pass filter in response to turbine torque disturbances. The results of the transfer function given in (5.33), were confirmed through the use of Matlab Simulink in order to identify the bode plot of the actual system. The bode plot of the actual system is shown in Fig. 5.10. The bode plot of the complete transfer function of (5.30) shows and confirms the low pass filter characteristic of the system. The cut-off frequency of the system is determined from the bode plot as 0.14 Hz. Finally, the proposed feedforward control principle can be understood from the system of Fig. 5.9 where it must be clear that the feedback-gain $1/R_d$ is not a constant, but it is adjusted by the duty cycle. Hence, MPP control of the system is in effect obtained by feedback-gain scheduling.

5.5 Simulated Results

In this section an analysis of the stability of the system as well as the dynamic behaviour of the system is further investigated. This analysis was achieved by simulating the dynamic response of the complete system for different inputs of wind speed frequency in MATLAB Simulink. For the first simulation, an average input wind speed of 8 m/s was chosen, where a 1 Hz sinusoidal-oscillating wind speed frequency was added to the wind speed input as shown in Fig. 5.11a. With this input wind signal at 1 Hz frequency, the resulting generator speed and duty cycle control are shown in Fig 5.11b. From this figure it can be seen that the duty cycle adjusts as the generator speed increases until steady state has been reached. For the second simulation the average input wind speed was chosen as 8 m/s again but now with a 0.01 Hz sinusoidal-oscillating wind speed frequency added to the wind speed input, as shown in Fig. 5.12a. With the 0.01 Hz wind speed input frequency, the simulated response of the duty cycle and the resulting generator speed are shown in Fig. 5.12b. Here, the much lower oscillation frequency is now visible in the duty cycle and generator speed. As the generator ramps up, it simply follows the changes in the fluctuating wind speed input. Both frequency results shown in Figs 5.11 and 5.12 prove that the system remains stable independent of wind speed frequency.

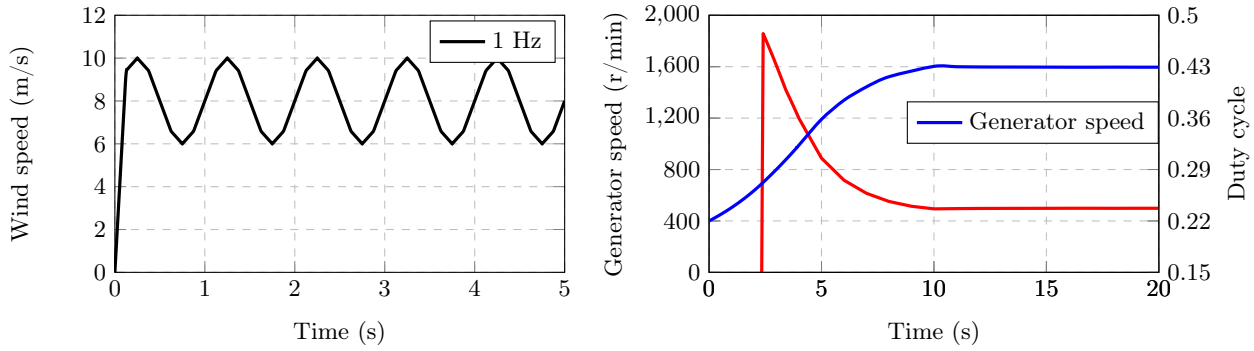

Figure 5.11: (a) Average input wind speed of 8 m/s at 1 Hz and (b) simulated response of generator speed(given initial speed of 400 r/min) and resulting duty cycle.

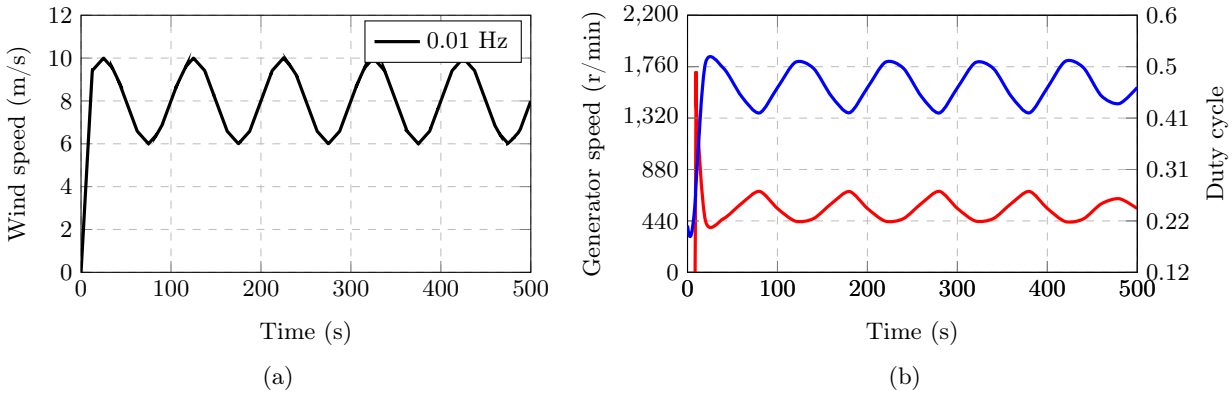

Figure 5.12: (a) Average input wind speed of 8 m/s at 0.01 Hz and (b) simulated response of generator speed(given initial speed of 400 r/min) and resulting duty cycle.

5.6 Conclusion

A simple and robust control method was proposed and evaluated for maximum power point tracking of DC-grid connected wind energy systems. The control method proposed in this chapter is based on the power-speed data of the turbine. The evaluation of the method shows that the proposed feedforward control of the duty cycle switching of the DC-DC converter works well in tracking the maximum power point of the system. This feedforward MPP control is essentially attained through feedback-gain scheduling.

The low sensitvity in the MPPT in response to large errors in the duty cycle and to DC-grid voltage variations are found, making the control robust against system parameter changes. In the case where the DC-grid voltage varies greatly, then the grid voltage in addition to the generator frequency can also be measured, whereby the proposed algorithm can still be used to update the duty cycle to its optimum value.

A new equivalent DC model for the PM generator and DC link load is introduced. From this model and dynamic system analysis, it is shown that the system is stable against wind speed disturbances. The system acts as a low pass filter with an overdamped response that is dominated by the efffective mechanical time constant of the system. The dominance of the mechanical time constant explains the stability robustness of the system against other system parameter changes.

Lastly, in this chapter it can be concluded that the practical implementation of the feed-forward control is simple since only the measurement of the generator-voltage's frequency (and the DC-grid voltage, if required) is necessary to determine the optimum duty cycle for MPPT. Hence, no PI-torque, speed and/or current regulator are necessary making the proposed control method attractive for industry.

Chapter 6

Practical Results

In this chapter, all the practical measurements and test results are documented and analysed for the proposed control method as put forward in the previous chapters. The practical tests were performed at the Stellenbosch University Electrical Machines Research Laboratory.

6.1 Practical Test Set-up

A practical test bench set-up for the practical measurements of the system is shown in Fig. 6.1. A simple block-diagram describing the system connections is given in Fig. 6.2. The test bench set-up included a 5 kW motor used to drive the 2.2 kW PM generator was coupled to the generator through the gearbox. A torque sensor is connected between the driving motor and the PM generator and is used to measure the input torque and speed. The PM generator is then connected to a full-bridge three-phase diode rectifier through a 3-phase switch. The DC output from the diode rectifier then forms the input to the DC-DC converter. The output of the DC-DC converter is then connected to the LC filter which in turn is then connected to the 48 V battery bank.

Thick copper wire cables, of approximately 15 mm, were used to make connections between the DC-DC converter's output, the LC filter and battery bank, to ensure that the cables were capable of handling the high current from the DC-DC converter. The following load connection circuit shown in Fig. 6.3 was made to connect the 48 V battery to the output of the DC-DC converter. This was done to ensure for gradual charging of the

capacitors and to allow for safe discharge of the capacitor and batteries when necessary by limiting the current. The circuit diagram shown in Fig. 6.3, shows the batteries connected as a load to the output of the DC-DC converter. The batteries are connected in series with a variable resistor of 50Ω and switch s_1, and further directly connected to the output of the DC-DC converter through switch s_2. A variable load resistor of 12Ω is connected across the batteries through switch s_3. The batteries always remain partly loaded in order to prevent over-charging.

To start up the system and take the measurements s1 is initially closed, and s_2 and s_3 are left open, in order to limit the current and gradually charge the capacitors of the DC-DC converter as the generator speed is slowly increased. Once the operating speed is reached, s_2 is then closed to have the 48 V of the batteries clamped to the output of the DC-DC converter. Thereafter, s_3 is closed and remains closed to discharge the batteries.

Figure 6.1: Generator and planetary gearbox on test bench set-up.

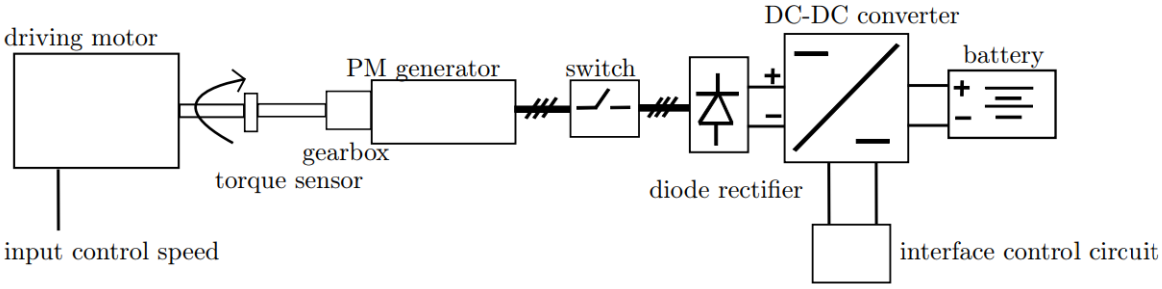

Figure 6.2: Layout of test bench set-up for practical measurements.

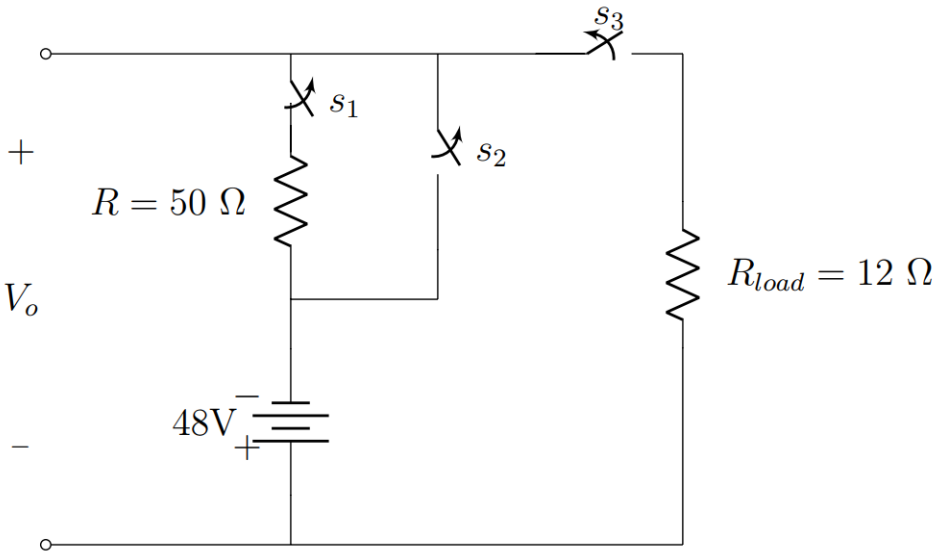

Figure 6.3: Circuit diagram of load connection.

6.2 Open-Circuit and Short-Circuit Test

6.2.1 Open-Circuit Test

The technique of the open circuit and short circuit tests were used to measure the PMSG model parameters and to determine the no-load performance of the machine. The first test performed on the generator was the open-circuit test. The terminals of the generator were left disconnected from any load. The speed of the driving machine was incrementally increased and the terminal voltage was measured at the various speeds. From this test, it was possible to plot the open-circuit characteristic (OCC) curve of the generator which is

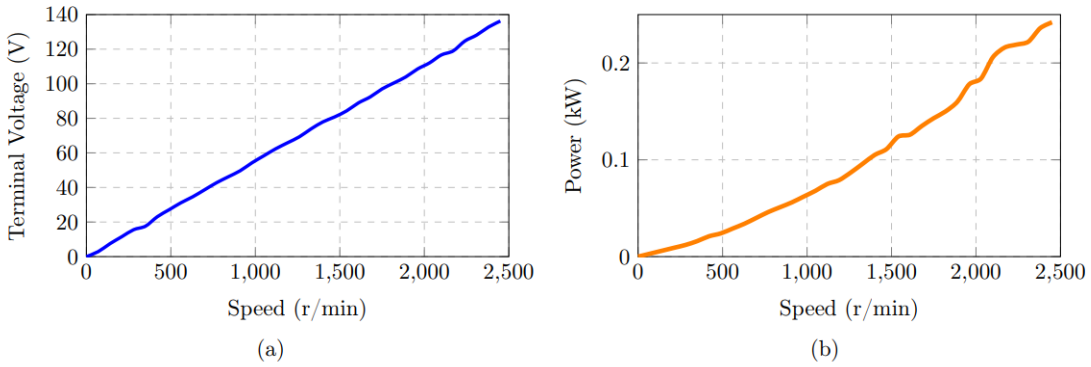

Figure 6.4: (a) OCC test terminal voltage versus generator speed and (b) no-load rotational losses versus generator speed.

shown in Fig. 6.4a. The figure shows the measured internal generated phase voltage of the generator plotted against rotational speed. As seen in the figure, the curve is linear due to fixed saturation since the PM flux remains fixed.

Furthermore, the no-load rotational losses of the generator were also measured. This is achieved from the mechanical input power that is required to drive the PMSG during the open-circuit test at no-load. These losses are made up of the friction and windage losses as well as the core losses. The curve showing the no-load rotational losses can be found in Fig. 6.4b, where the power is plotted against the rotational speed.

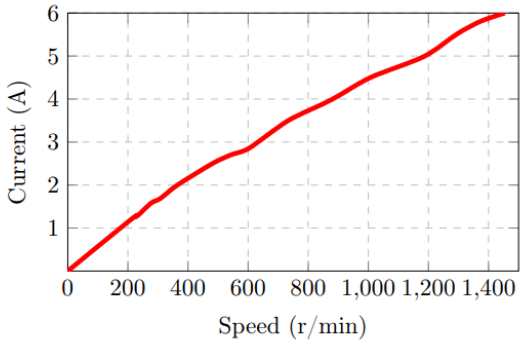

Figure 6.5: SCC current versus generator speed.

6.2.2 Short-Circuit Test

The second test performed on the generator was the short-circuit test. To conduct the short-circuit test, the terminals of the PMSG were connected to a balanced three-phase wye connected load of 8.1Ω. The line current was measured as the rotational speed was gradually increased. The measurements were taken till the rated current of 6 A was reached. From this test, the short-circuit characteristic (SCC) curve was obtained as shown in Fig. 6.5. The figure shows that the curve is nonlinear since the synchronous reactance varies with frequency.

6.2.3 PMSG Machine Parameters

The data obtained from the OCC and SCC tests were used to determine the machine parameters. The stator resistance was measured with a multimeter between two phase of the output terminals of the PM generator and was determined by

$$R_s = \frac{R_{LL}}{2}, \tag{6.1}$$

where R_{LL} is the line-line resistance measured between two phases. The value measured for the stator resistance was $R_s = 1.15\Omega$. The synchronous reactance is determined from the open-circuit and short-circuit test measurements at a specific speed. From the tests, the per phase impedance is determined by

$$Z = \frac{E_{oc}}{I_{sc}}, \tag{6.2}$$

where E_{oc} is the phase induced voltage determined from the open-circuit test and I_{sc} is the short-circuit current. From this, the magnitude of the synchronous reactance is calculated by

$$X_s = \sqrt{Z^2 - R^2}, \tag{6.3}$$

Lastly, the inductance of the PM generator is given by

$$L_s = \frac{X_s}{2\pi f_x}, \tag{6.4}$$

Table 6.1: Practical Machine Parameters Compared to Simulated Results.

Machine Parameter	Practical	Simulated
R_s Ω	1.15	1.13
L_s mH	28	22
λ_m Wb	0.257	0.36

where f_x is the frequency. From the no-load rotational losses given in the Fig. 6.4b. and from the equation given by (5.2), the mechanical damping coefficient of the PM generator was determined. This was determined at the rated operating point of the machine and resulted in $B = 0.0036$ N.m.s/rad which is compared to the value $B = 0.007$ used in Chapter 5. The machine parameters obtained from the practical measurements of the SEW-EURODRIVE 2.2 kW generator are compared to those obtained from FEA simulation in Chapter 3 and are tabulated in Table 6.1.

6.3 DC-DC Converter

The DC-DC converter used for the system is shown in Fig. 6.6. An interface circuit was required to power and drive the IGBT switches of the Intelligent Power Module (IPM) which is an advanced hybrid power device. The interface PCB circuit used as the interface circuit is shown in Fig. 6.7. The interface circuit comprised of an isolated DC power supply. This isolated DC power supply is required to supply a constant output voltage of 15 V which is required to power the IPM. An Arduino micro-controller is used to generate a PWM signal at the specified switching frequency of 10 kHz. The micro-controller is also used to set the duty cycle value at which the PWM signal is produced. Further, the micro-controller is used to adjust the duty cycle range through the use of a 100 kΩ variable resistor in order to obtain the desired duty cycle value. The measured PWM signal generated from the micro-controller is shown in Fig. 6.8. From this figure, it can be seen that

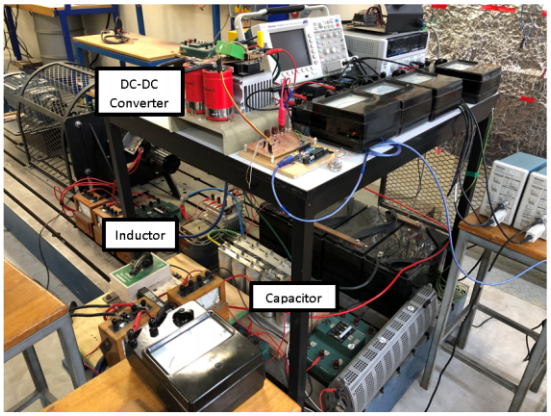

Figure 6.6: DC-DC converter and LC filter.

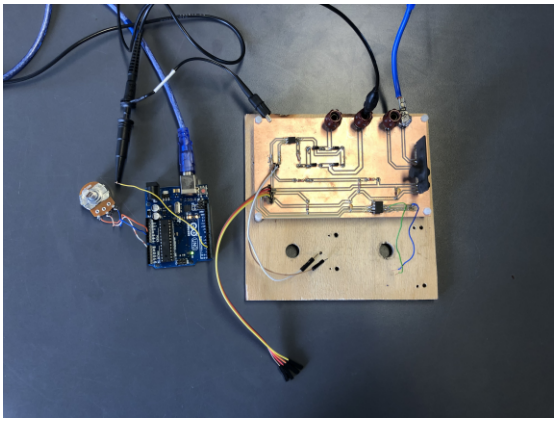

Figure 6.7: Interface circuit used to power and control the DC-DC converter.

the micro-controller generates a PWM signal with a duty cycle of 49 % , at a frequency of 10 kHz and voltage of 1.5 V.

The PWM signal obtained from the micro-controller then forms the input signal for the opto-coupler which forms part of the interface circuitry. The opto-coupler is used to isolate the PWM signal from the gate signal that is required to trigger the IGBT switches. The output signal of the opto-coupler is connected to the gate signal pin of the IPM. The gate signal for the IPM was measured and is shown in Fig. 6.9. The frequency of this signal is at the correct required value of 10 kHz and the correct voltage of 4.88 V that is required to power the pin of the gate driver.

The output signal of the DC-DC converter was measured to confirm that the DC-DC converter was operating as expected and that the interface circuit was capable of triggering the IGBT switch. The waveform of this output is given in Fig. 6.10, where the output voltage of the DC-DC converter (measured across the diode), the inductor current and battery current are plotted against time. From Fig. 6.10, it can be seen that the DC-DC converter functioned as expected. Figure 6.11 shows the case when the DC-DC converter is operating under discontinuous-conduction mode, where the output current is less than the critical inductor current level. During this stage, the inductor current is equal to zero for a portion of the cycle. From this figure it can be seen that there is resonance that occurs when the inductor current falls to zero. This ringing (resonance) seen in the diode voltage and inductor current can be minimized through the use of snubber capacitors or a dumping resistor.

Once accurate functionality of the DC-DC converter was confirmed, it was then connected to the LC filter which is then connected to the DC-grid modelled by the battery bank.

6.4 Complete System Measurements

The MPPT control method proposed in Chapter 5 was practically tested on the system in the Electrical Machine Laboratory. In Chapter 5, the control method was developed and evaluated for a 8-pole, 5 kW PM generator that was designed in Chapter 4. For the practical test, the MPPT control method was tested on the commercial 6-pole, 2.2 kW PM generator simulated in Chapter 3.

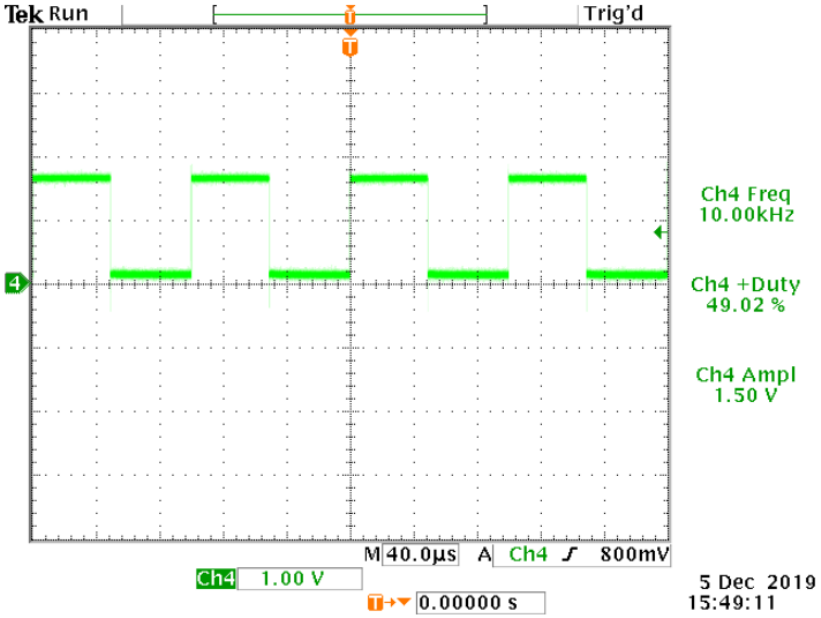

Figure 6.8: PWM signal with 50 % duty cycle at 10 kHz switching frequency.

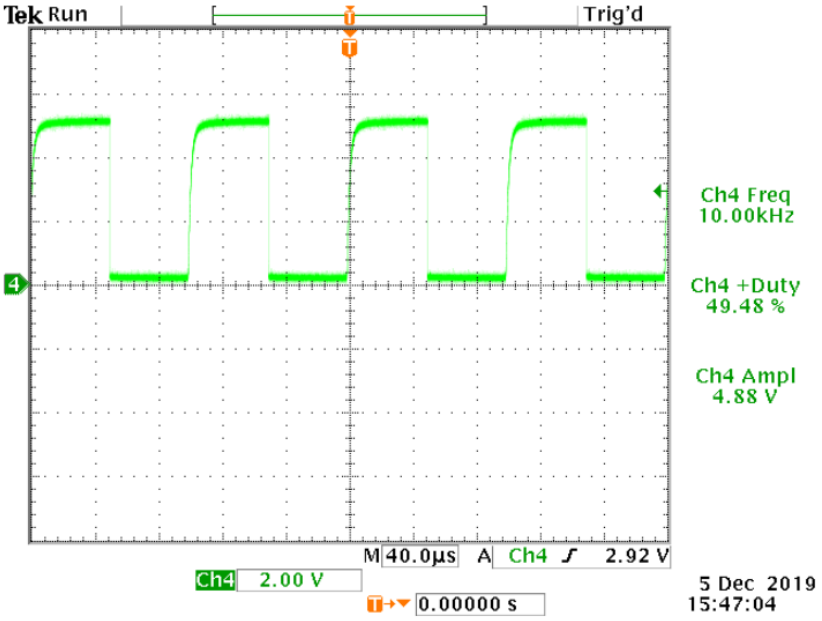

Figure 6.9: Gate signal input to IPM.

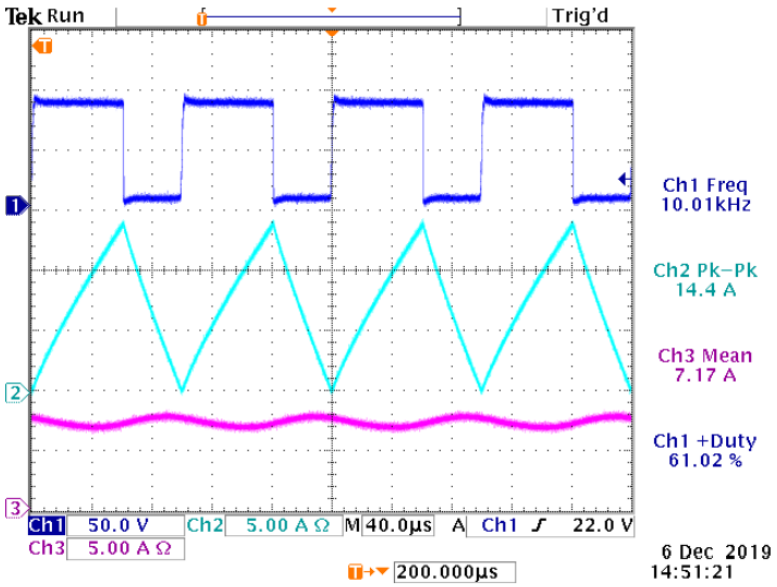

Figure 6.10: Measurement of the diode voltage, inductor current and battery current from output side of DC-DC converter.

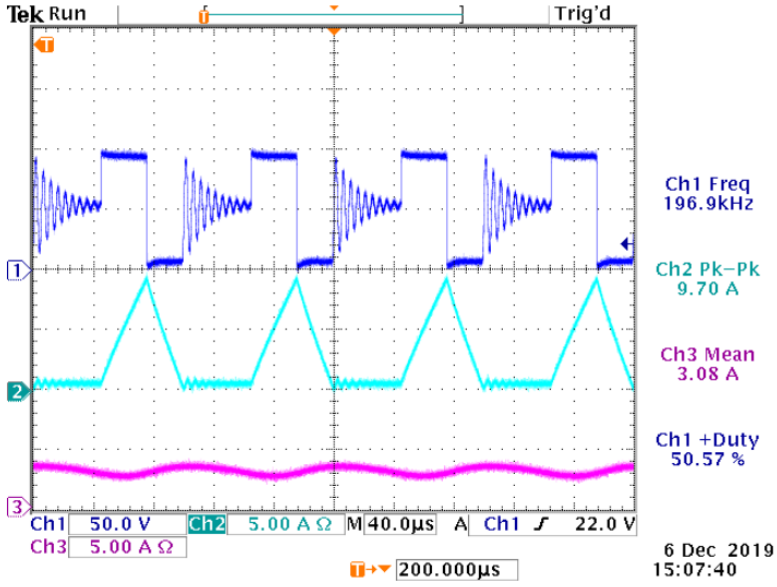

Figure 6.11: Discontinuous-conduction mode of DC-DC converter.

The duty cycle values required to have the turbine of the system operating at its MPPT were determined by following the method described in Chapter 5. For this specific system, the power angle δ calculated from (5.7) cannot be greater than 45^o, forming the stability limit. In the instance when δ is greater than 45^o for the MPPT duty cycle calculation for this system, the turbine operating point was made to lie further along the turbine power curve at a higher speed. The optimum duty cycle function that was calculated at a specific mechanical speed for the system is given in Fig. 6.12. Hence, for this partcular system, there are instances when the turbine cannot operate at its MPPT trajectory.

To investigate whether the system could be controlled by adjusting the duty cycle of the DC-DC converter, the duty cycle values from Fig. 6.12 were used to control the DC-DC converter. A motor-drive was controlled to emulate the wind turbine for the purpose of driving the generator. The motor-drive was controlled to run at set speeds of the wind turbine, as obtained from the power curves for the various wind speeds. Further practical investigation needs to be done to have the motor truly emulating the behaviour of the wind turbine in response to the dynamics of changes in wind speed. For the measurements, the PM generator was driven to a specific speed at which the duty cycle was calculated for. At each operating point of the speed, a measurement of the turbine power, output current and output voltage were taken. The input power of the generator and the output power measured at the output of the DC-DC converter were then measured and are shown in

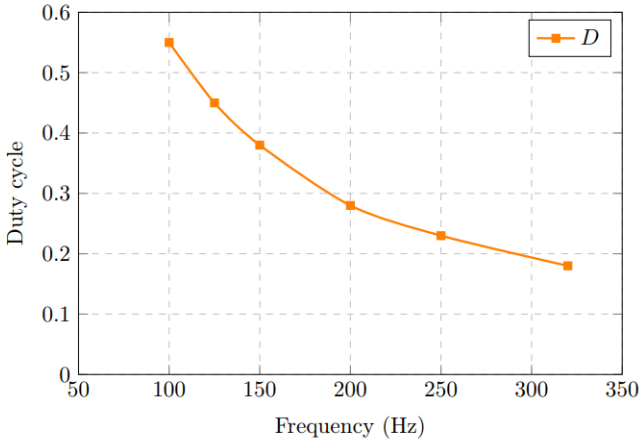

Figure 6.12: Duty cycle function calculated for the practical system.

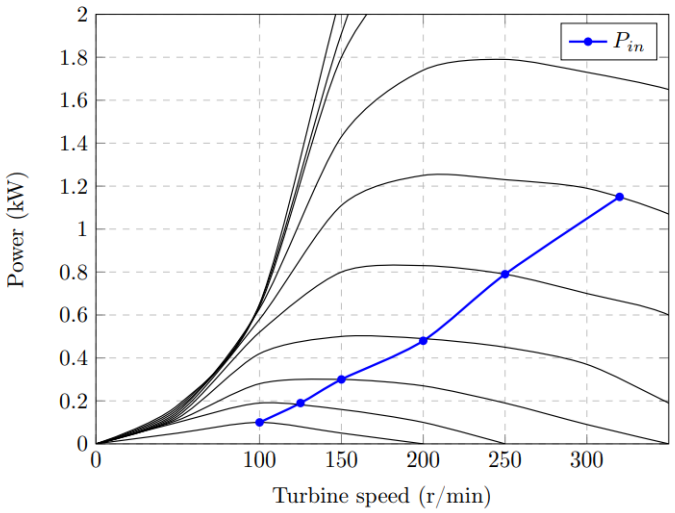

Figure 6.13: Measured input power and output power versus turbine speed.

Fig. 6.13.

6.5 Further Practical Measurements

Further practical measurements were taken of the system. The value of the filter inductor of the DC-DC converter was increased from 180 uH to 900 uH. The results of the new

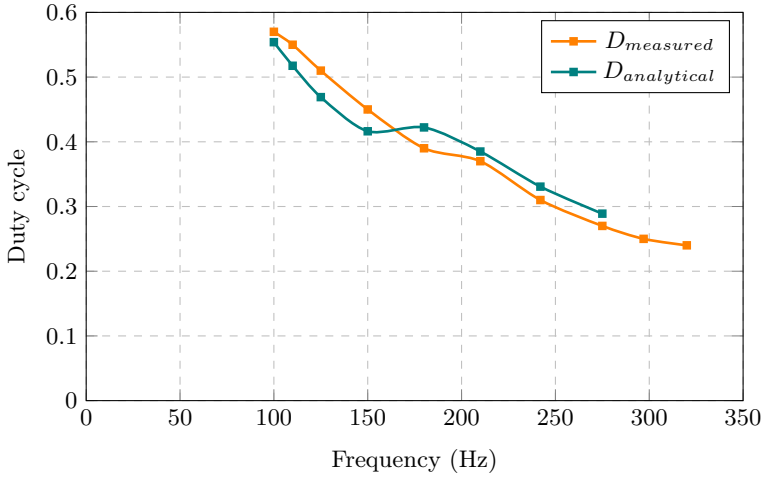

Figure 6.14: Optimum duty cycle function calculated with and withou losses.

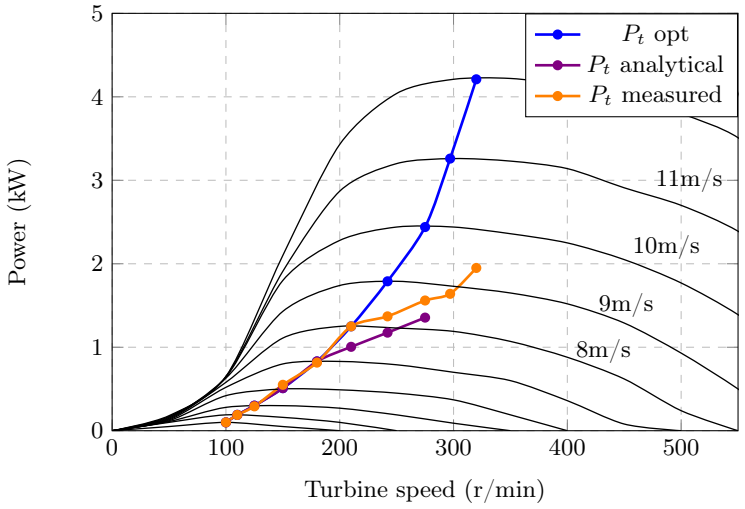

Figure 6.15: Simulated steady state operating turbine power versus turbine speed with ± 0.1 pu dc-grid voltage variation.

measurements taken are shown in Figures 6.14 and 6.15. Firstly the optimum duty cycle values were determined analytically using the calculations discussed in Section 5.2 and the results of $D_{analytical}$ are shown in Fig. 6.14. The duty cycle values that are required to have the system run at the optimum turbine power P_t opt values was deternined manually, thus obtaining $D_{measured}$ as shown in Fig. 6.14. The $D_{measured}$ values were then used to compare with the duty cycle values that were determined analytically. From this, the turbine power was measured by adjusting the duty cycle of the DC-DC converter according to the analytical duty cycle values. The results of P_t measured and P_t anaytical is shown in Fig 6.15. With the changes made to the inductor value, the results revealed a decrease in the current ripple of the DC-DC converter and an improved tracking of the MPPT points. The first few points are tracked accuratelly before a deviation occurs due to limiting boundaries of the power angle *delta*.

6.6 Conclusion

In this Chapter, the practical measurements and tests were conducted on the different components of the system. The machine parameters of the practical PM generator were determined. The interface driver circuitory was capable of powering and driving the DC-DC converter and functioned as expected. The results from the practical measurements

show that the DC-DC converter is capable of controlling the turbine to run at its maximum turbine power by adjusting the duty cycle value. The results shown in Fig. 6.13 show that the turbine slides along its power point trajectory, however not at its maximum power points because of the restriction from the power angle limit. Further investigation is required to have the turbine operating at its MPPT, by taking consideration of the power angle limit in the development of the duty cycle function calculations.

Chapter 7

Conclusion and Recommendations

7.1 Conclusion

In this study a FE simulation analysis of an existing generator was conducted and compared using two FE software programs. An alternative PMSG generator was designed under the motivation of improving the cogging torque of the generator. A simple control method that achieves maximum power point tracking of DC-grid connected wind energy systems was proposed and evaluated. Lastly, tests and measurements were conducted on a practical set-up of the system.

The results of the FE analysis obtained in this study showed that the simulation implemented to model the commercial SEW-EURODRIVE 6-pole, 2.2 kW PM generator is tolerable accuracy. The results of the simulated torque obtained from the FE analysis was 8.9 Nm, which was close to the rated torque of the existing machine of 9 Nm. The simulation results obtained from SEMFEM compared well to those obtained from the commercial ANYSYS Maxwell FEA software.

The design of an alternative 8-pole, 4.2 kW PM generator with FEA was done. The PM wind generator was designed with fractional-slot windings for fixed-pitch wind turbines. A generator design with a increased number of poles was chosen in order to increase the power density. Achieving low cogging torque was furthermore of importance in the design.

The evaluation of the control method proposed for MPPT of the system showed that

the proposed method is successful. The control method put forward was achieved through a form of feedback-gain scheduling. From the steady state system analysis, an equation was derived to determine the necessary duty cycle occurring at each of the maximum turbine power operating points, at the corresponding generator speed. It was found that the MPPT control method has low sensitivity to large errors introduced in the duty cycle function and to variations in the DC-grid voltage. Furthermore, from the dynamic system analysis it was shown that the system remains stable against disturbances in the wind speed. Furthermore, the system acts as a low pass filter with an overdamped response which was attributed to the dominance of the effective mechanical time constant of the system. This was confirmed with the Bode plot presented in Chapter 5.

The measurements obtained from the practical set-up of the system, showed that MPPT of the system can be achieved through the control of the duty cycle of the DC-DC converter with the duty cycle values calculated as proposed in Chapter 5, however consideration of power angle limit must be taken into consideration. In this case the duty cycle is used to have the system operate along the turbine power curve at higher speeds.

7.2 Recommendations

As concluded in this chapter, the system proposed in this thesis works well. Future recommendations to improve the system as it is now and to further investigate other aspects of the system are:

1. The LC filter of the DC-DC converter must be redesigned by determining a higher inductor value to reduce the inductor current ripple which stands at quite a high percentage of 22%.

2. A new PM generator with a higher power density must be used to replace the smaller commercial PM generator, used in the study, in order to reach the rated capacity of the turbine.

3. The system proposed in this study must, after redesign, be put up on an actual wind site/farm. Automation of the duty cycle control is also proposed. This can be achieved by measuring the frequency of the generator or the DC-link voltage, in

determing the specific duty cycle by means of the micro-controller. Lastly, a practical investigation on the impact of wind speed variations on the stability of the system.

Appendices

Appendix A

Generator CAD Drawings

A 2-D CAD drawing of the stator laminations of the commercial SEW-EURODRIVE generator is shown in Fig. A.1. A CAD drawing of the surface mounted permanent magnet generator rotor is shown in A.2 and the 3-D CAD drawing of this is given in Fig. A.3.

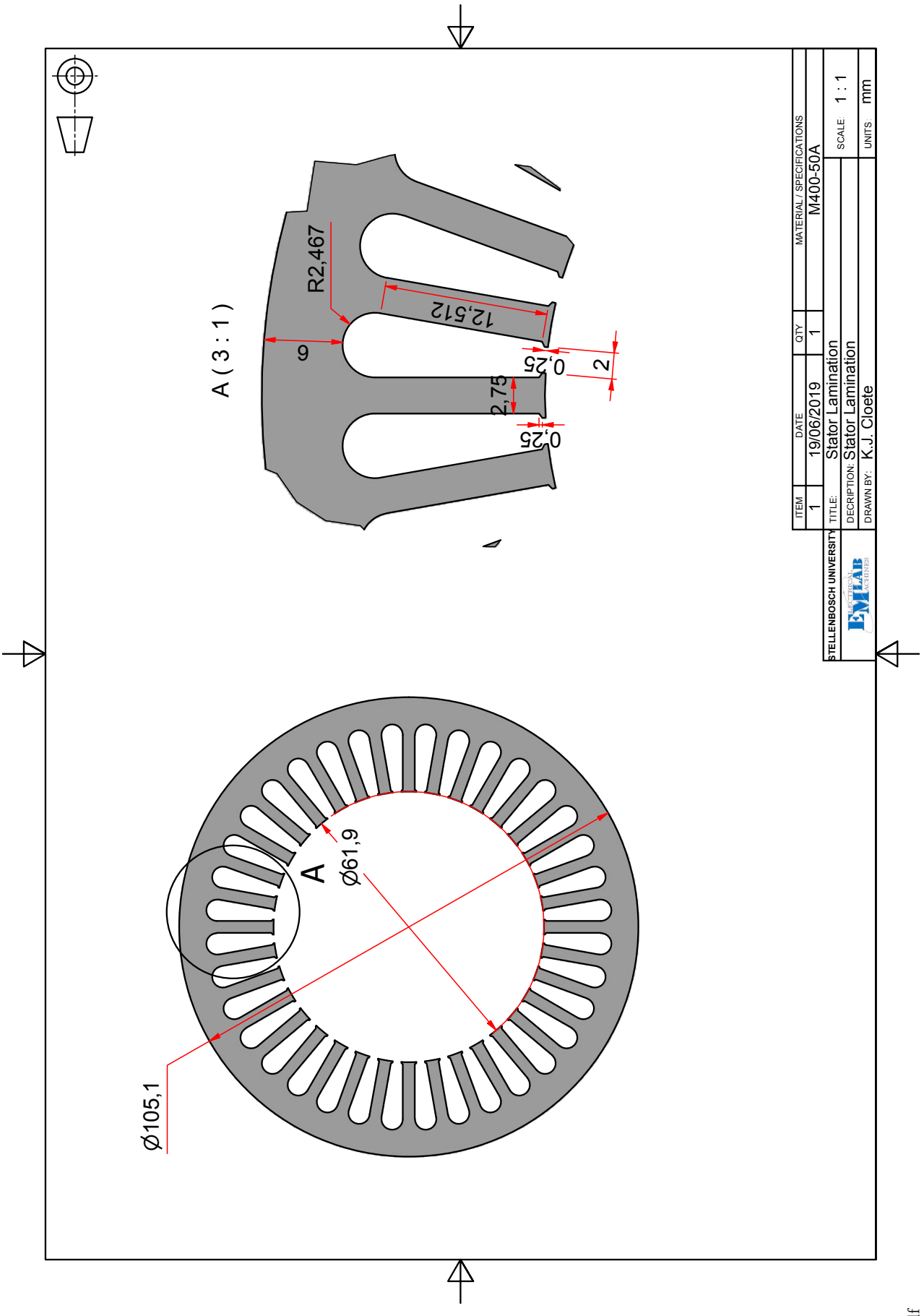

amination.pdf

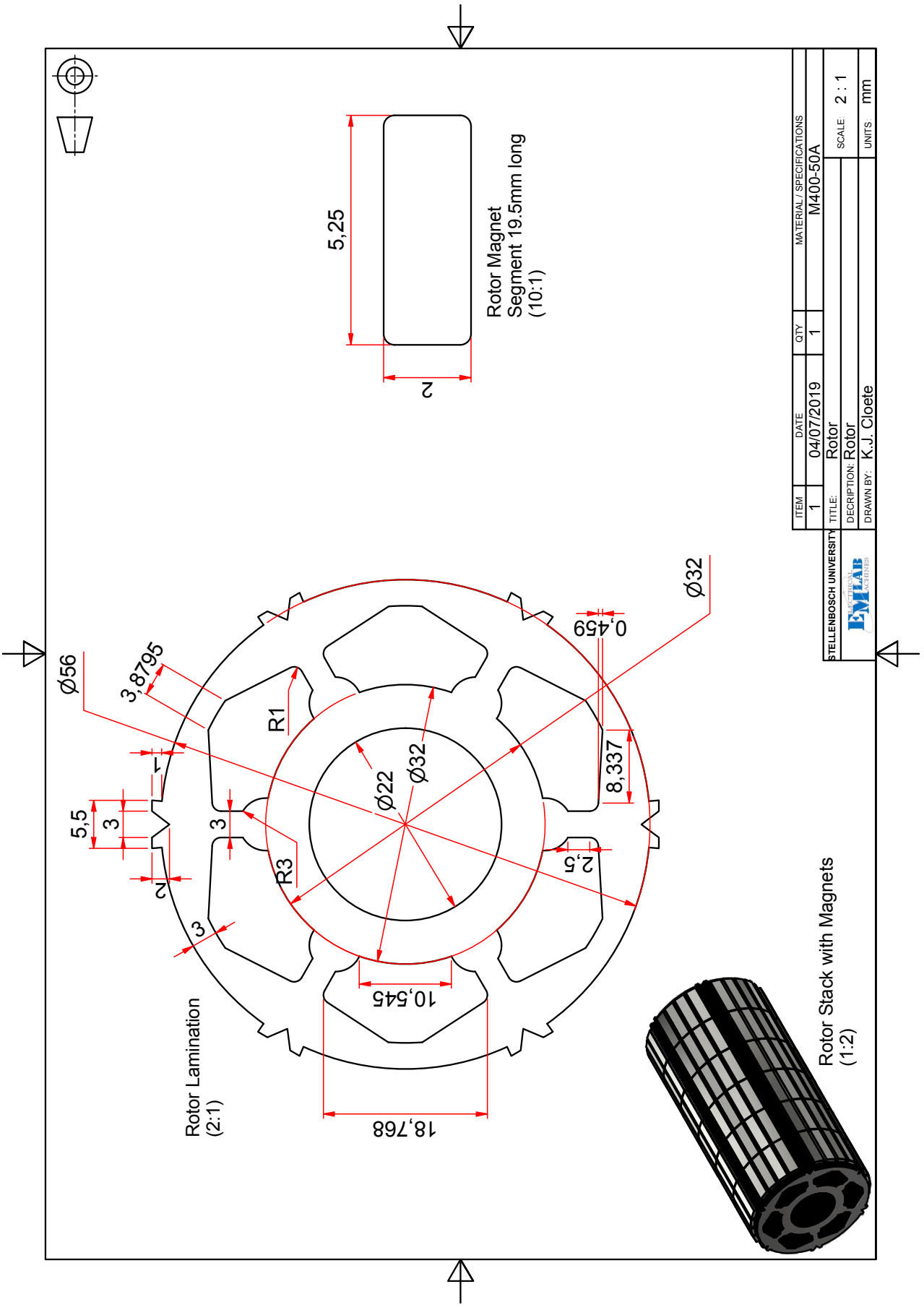

Figure A.2: 2-D CAD drawing of generator rotor.

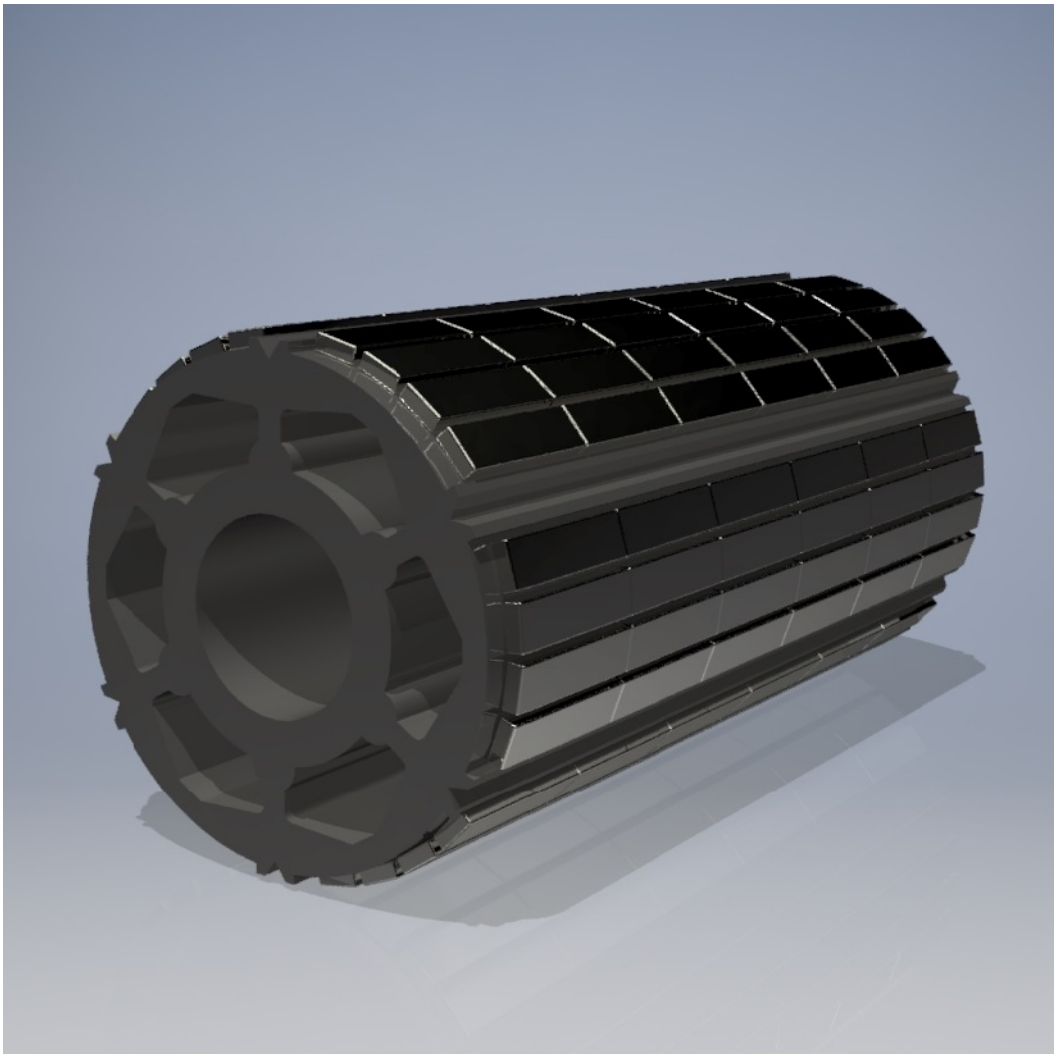

Figure A.3: 3-D CAD drawing of surface mounted permanent magnet generator rotor.

Bibliography

[1] Masters, G.M.: *Renewable and efficient electric power systems*. John Wiley & Sons, 2013.

[2] Renewables, R.: Global status report. *Renewable Energy Policy Network for the 21st Century*, 2019.

[3] Alnasir, Z. and Kazerani, M.: An analytical literature review of stand-alone wind energy conversion systems from generator viewpoint. *Renewable and Sustainable Energy Reviews*, vol. 28, pp. 597–615, 2013.

[4] Pombo-van zyl, N.: Tracking wind energy in south africa. *ESI Africa- Africa's Power Journal*, vol. 4.

[5] Council, G.W.E.: Global wind report. 2019. *Brussels: GWEC*, 2019.

[6] El Chaar, L., Lamont, L. and Elzein, N.: Wind energy technology industrial update. In: *2011 IEEE Power and Energy Society General Meeting*, pp. 1–5. IEEE, 2011.

[7] Thakur, A., Panigrahi, S., Behera, R. *et al.*: A review on wind energy conversion system and enabling technology. In: *2016 International Conference on Electrical Power and Energy Systems (ICEPES)*, pp. 527–532. IEEE, 2016.

[8] Nouh, A. and Mohamed, F.: Wind energy conversion systems: Classifications and trends in application. In: *2014 5th International Renewable Energy Congress (IREC)*, pp. 1–6. IEEE, 2014.

[9] Huang, C., Li, F. and Jin, Z.: Maximum power point tracking strategy for large-scale wind generation systems considering wind turbine dynamics. *IEEE Transactions on Industrial Electronics*, vol. 62, no. 4, pp. 2530–2539, April 2015. ISSN 1557-9948.

[10] Dalala, Z.M., Zahid, Z.U., Yu, W., Cho, Y. and Lai, J.: Design and analysis of an mppt technique for small-scale wind energy conversion systems. *IEEE Transactions on Energy Conversion*, vol. 28, no. 3, pp. 756–767, Sep 2013. ISSN 1558-0059.

Figure 1: Bibliography

[11] Ahshan, R., Al-Badi, A., Hosseinzadeh, N. and Shafiq, M.: Small wind turbine systems for application in oman. In: *2018 5th International Conference on Electric Power and Energy Conversion Systems (EPECS)*, pp. 1–6. April 2018. ISSN null.

[12] Abkar, M.: Theoretical modeling of vertical-axis wind turbine wakes. *Energies*, vol. 12, no. 1, p. 10, 2019.

[13] Das, A., Chimonyo, K.B., Kumar, T.R., Gourishankar, S. and Rani, C.: Vertical axis and horizontal axis wind turbine-a comprehensive review. In: *2017 International Conference on Energy, Communication, Data Analytics and Soft Computing (ICECDS)*, pp. 2660–2669. IEEE, 2017.

[14] Stegmann, J. and Kamper, M.: Economic and efficiency evaluation of different battery charging wind generator systems. In: *Southern African Universities Power Engineering Conference (SAUPEC), Johannesburg, South Africa, Citeseer*. Citeseer, 2010.

[15] Mansour, M., Mansouri, M. and Mimouni, M.: Comparative study of fixed speed and variable speed wind generator with pitch angle control. In: *2011 International Conference on Communications, Computing and Control Applications (CCCA)*, pp. 1–7. IEEE, 2011.

[16] Muljadi, E., Butterfield, C.P. and Yih-Huie Wan: Axial-flux modular permanent-magnet generator with a toroidal winding for wind-turbine applications. *IEEE Transactions on Industry Applications*, vol. 35, no. 4, pp. 831–836, July 1999. ISSN 1939-9367.

[17] Karim, N.A., Azzouzi, J. and Barakat, G.: Influence of skewing on the performances of an axial flux pm wind generator coupled to a diode rectifier. In: *2007 IEEE International Electric Machines Drives Conference*, vol. 2, pp. 1037–1042. May 2007. ISSN null.

[18] Ali, R.B., Schulte, H. and Mami, A.: Modeling and simulation of a small wind turbine system based on pmsg generator. In: *2017 Evolving and Adaptive Intelligent Systems (EAIS)*, pp. 1–6. IEEE, 2017.

[19] Sl-Subhi, A., Alsumiri, M. and Alalwani, S.: Novel mppt algorithm for low cost wind energy conversion systems. In: *2017 Intl Conf on Advanced Control Circuits Systems (ACCS) Systems & 2017 Intl Conf on New Paradigms in Electronics & Information Technology (PEIT)*, pp. 144–148. IEEE, 2017.

[20] Kanda, T., Mdakane, L., Labuschagne, C. and Kamper, M.: Dynamics of maximum power point wind energy battery charging systems. In: *2019 Southern African Universities Power Engineering Conference/Robotics and Mechatronics/Pattern Recognition Association of South Africa (SAUPEC/RobMech/PRASA)*, pp. 576–581. IEEE, 2019.

Figure 2: Bibliography

[21] Plooy, J.-P.D.: Development of a converter-fed reluctance synchronous generator wind turbine controller. 2015.

[22] Botha, C.D.: Variable speed and torque control of a wind turbine system with assisted reluctance synchronous generator technology. 2018.

[23] Rossouw, F.G.: *Analysis and design of axial flux permanent magnet wind generator system for direct battery charging applications.* Ph.D. thesis, Stellenbosch: University of Stellenbosch, 2009.

[24] Mohan, N., Undeland, T.M. and Robbins, W.P.: *Power electronics: converters, applications, and design.* John wiley & sons, 2003.

[25] Muljadi, E., Drouilhet, S., Holz, R. and Gevorgian, V.: Analysis of wind power for battery charging. Tech. Rep., National Renewable Energy Lab., Golden, CO (United States), 1995.

[26] Heydari, M. and Smedley, K.: Comparison of maximum power point tracking methods for medium to high power wind energy systems. In: *2015 20th Conference on Electrical Power Distribution Networks Conference (EPDC)*, pp. 184–189. IEEE, 2015.

[27] Esmaili, R., Xu, L. and Nichols, D.: A new control method of permanent magnet generator for maximum power tracking in wind turbine application. In: *IEEE Power Engineering Society General Meeting, 2005*, pp. 2090–2095. IEEE, 2005.

[28] Pan, T., Ji, Z. and Jiang, Z.: Maximum power point tracking of wind energy conversion systems based on sliding mode extremum seeking control. In: *2008 IEEE Energy 2030 Conference*, pp. 279–283. IEEE, 2008.

[29] Koutroulis, E. and Kalaitzakis, K.: Design of a maximum power tracking system for wind-energy-conversion applications. *IEEE transactions on industrial electronics*, vol. 53, no. 2, pp. 486–494, 2006.

[30] Pribadi, K.D., Wijaya, F.D. *et al.*: Dynamic response of maximum power point tracking using particle swarm optimization for wind energy conversion system. In: *2016 8th International Conference on Information Technology and Electrical Engineering (ICITEE)*, pp. 303–308. IEEE, 2016.

[31] Liang, D., Qin, C., Wang, S. and Guo, H.: Reliability evaluation of dc distribution power network. In: *2018 China International Conference on Electricity Distribution (CICED)*, pp. 654–658. IEEE, 2018.

Figure 3: Bibliography

[32] Aswat, M., Dangor, M.R.E. and Cronje, W.: A standalone personal consumer grid for rural household electrification. In: *2019 Southern African Universities Power Engineering Conference/Robotics and Mechatronics/Pattern Recognition Association of South Africa (SAUPEC/RobMech/PRASA)*, pp. 487–492. IEEE, 2019.

[33] Binbin, Z., Minxiao, H. and Xiao, C.: Research on the directly driven permanent magnet synchronous generator connected to dc grid. 2013.

[34] Qi, L., Pan, J., Liljestrand, L., Backman, M., Antoniazzi, A., Raciti, L. and Riva, M.: Dc power distribution: New opportunities and challenges. In: *2017 IEEE Second International Conference on DC Microgrids (ICDCM)*, pp. 40–46. IEEE, 2017.

[35] Mitra, P., Hanning, J., Köhlström, J., Larsson, T. and Danielsson, J.: Dc grid system behavior: A real-time case study. In: *2015 IEEE Power & Energy Society General Meeting*, pp. 1–5. IEEE, 2015.

[36] Pan, T., Ji, Z. and Jiang, Z.: Maximum power point tracking of wind energy conversion systems based on sliding mode extremum seeking control. In: *2008 IEEE Energy 2030 Conference*, pp. 1–5. IEEE, 2008.

[37] Studer, C., Keyhani, A., Sebastian, T. and Murthy, S.: Study of cogging torque in permanent magnet machines. In: *IAS'97. Conference Record of the 1997 IEEE Industry Applications Conference Thirty-Second IAS Annual Meeting*, vol. 1, pp. 42–49. IEEE, 1997.

[38] Umans, S.D.: *Fitzgerald and Kingsley's electric machinery*. McGraw-Hill Higher Education, 2013.

[39] Kamper, M.: *Design Optimisation of Cageless Flux Barrier Rotor Reluctance Synchronous Machine*. PhD, University of Stellenbosch, 1996.

[40] Stegmann, J.A. and Kamper, M.J.: Design aspects of double-sided rotor radial flux air-cored permanent-magnet wind generator. *IEEE Transactions on Industry Applications*, vol. 47, no. 2, pp. 767–778, 2011.

[41] Vorster, C.W.: *Design of a reluctance synchronous machine for an electric vehicle with a multi speed gearbox*. Ph.D. thesis, Stellenbosch: Stellenbosch University, 2014.

[42] Mnati, M.J., Abed, J.K., Bozalakov, D.V. and Van den Bossche, A.: Analytical and calculation dc-link capacitor of a three-phase grid-tied photovoltaic inverter. In: *2018 IEEE 12th International Conference on Compatibility, Power Electronics and Power Engineering (CPE-POWERENG 2018)*, pp. 1–6. April 2018. ISSN 2166-9546.

Figure 4: Bibliography